



Novel Cu-Fe bi-metal oxide quantum dots coupled g-C₃N₄ nanosheets with H₂O₂ adsorption-activation trade-off for efficient photo-Fenton catalysis

Mingen Liu, Hong Xia^{*}, Wenxin Yang, Xiaoyu Liu, Jiao Xiang, Xiaoming Wang, Liangsheng Hu, Fushen Lu^{*}

Department of Chemistry and Key Laboratory for Preparation and Application of Ordered Structural Materials of Guangdong Province, Shantou University, Guangdong 515063, China

ARTICLE INFO

Keywords:

0D/2D hybrids
Adsorption-activation trade-off
Multiple synergies
Photo-Fenton
Wastewater treatment

ABSTRACT

Exploitation of catalysts with multi-active sites is very important for enhancing catalytic performance. 0D/2D hybrids, especially quantum dots (QDs)/nanosheets (NSs), have attracted increasing attentions for advanced oxidation processes due to high charge mobility and more active sites. However, 0D/2D hybrids with multi-active sites still remain a great challenge. Herein, 0D Cu-Fe bi-metal oxide QDs/2D g-C₃N₄ (CNNs) exhibiting superior advantages beyond single-metal 0D/2D counterparts was fabricated via a facile one-step synthesis strategy for photo-Fenton catalysis. The synergy of ultrafine Cu-Fe sites on CNNs led to outstanding tetracycline removal efficiency over a wide pH range. Our experiments and DFT calculations clearly demonstrated that except for the fast charge separation and transfer, this synergy could achieve the optimal H₂O₂ adsorption-activation trade-off on Cu-Fe sites, while also modify tetracycline absorption, leading to multiple synergies of adsorption-catalytic degradation and photocatalysis-Fenton oxidation. This work provides new insights in developing multi-functional 0D/2D hybrids for environment and energy applications.

1. Introduction

Environmental issues caused by the extensive use of refractory organic compounds such as personal care products, pesticides, dyes and other industrial chemicals, are becoming more and more serious, which has posed threats to human health and seriously restricted the sustainable development of our society [1–3]. Most of these organic pollutants, even at trace concentrations, are usually harmful and highly toxic to human beings, even endocrine disruptive, teratogenic and potentially carcinogenic. Therefore, the removal of organic pollutants has become a very urgent task.

Advanced oxidation processes (AOPs), especially Fenton oxidation, as a hot-spot method for the treatment of water pollution, have excellent catalytic performance in treating organic pollutants by highly active radicals such as hydroxyl radicals (•OH), superoxygen radicals (O₂^{•−}), singlet oxygen (¹O₂) and sulfate radicals (SO₄^{•−}) generated from the decomposition of oxidizing agents [4–8]. In the classical Fenton system, iron oxide nanoparticles (NPs) have been widely applied as heterogeneous catalysts due to high enrichment in nature, low cost, and weak toxicity. However, slow conversion of Fe(III)/Fe(II) and strict pH

requirement limit the activity of iron-based Fenton catalysts [9,10]. To overcome the limitation of iron-based catalysts, catalysts with dual active sites have received significant attentions [11–15]. Karthikeyan et al. reported that Fe and Cu oxides dispersed on SBA-15 exhibited better catalytic activity than that of single-oxide counterparts for *N*, *N*-diethyl-*p*-phenyl diamine degradation due to a faster Fe³⁺/Fe²⁺ conversion via the reduction by Cu⁺ [11]. Wan et al. synthesized Fe₃O₄-Mn₃O₄/RGO hybrids for highly activating H₂O₂ to degrade sulfamethazine [13]. Efficient regeneration of Mn²⁺ caused by surface Fe²⁺ led to the remarkable increase in catalytic activity. Although some exciting advances have been achieved in these catalysts with dual active sites, the aggregated and large nanoparticles significantly lower the available surface sites. Moreover, random dispersion and irregular morphology of these polymetallic oxide caused insufficient exploitation of the nanostructures and the uncertainty of the synergies of multi-active sites. Therefore, there is still great room for the further improvement of catalytic performance by tailoring the morphology of polymetallic oxide NPs in composites. Nevertheless, it is also a great challenge to explore simple methods for exploiting of advanced catalysts with multi-active sites. In addition, there has been an unfortunate lack of in-depth

^{*} Corresponding authors.

E-mail addresses: xiahong@stu.edu.cn (H. Xia), fslu@stu.edu.cn (F. Lu).

<https://doi.org/10.1016/j.apcatb.2021.120765>

Received 1 July 2021; Received in revised form 14 September 2021; Accepted 26 September 2021

Available online 28 September 2021

0926-3373/© 2021 Elsevier B.V. All rights reserved.

research on synergistic mechanism of multi-metallic sites. Current reports primarily focused on the regeneration of low-valence metal species in AOPs by the synergy of multi-metallic sites [11]. However, how multi-metal sites influence synergistically the reactivity of oxidants (H_2O_2 or PMS) involved in Fenton process, especially the adsorption and activation of them on active sites are ignored and have not yet been elucidated, which is very critical and worthy of exploration.

To maximize the catalytic activity and atom utilization, catalysts with different microstructures ranging from crystal to amorphous structure, quantum dots (QDs) to single atom, have been recently explored. It is found that the fabrication of 0D QDs or clusters is demonstrated to be a promising strategy, because they have small lateral size and abundant surface defects, permitting to offer affluent active sites for catalysis. Currently, 0D QDs/2D nanosheets (NSs) hybrids have been significantly developed due to the fact that the interactions between two moieties can make QDs more dispersive and stable [16–19]. 0D/2D photocatalysts have also been reported [20–23]. For example, Fang et al. [20] and Xiao et al. [21] respectively loaded CdS QDs onto graphene NSs, leading to an obviously enhanced photocatalytic and PEC performance in comparison with CdS nanocomposites. However, the largely consumed graphene NSs (volume ratio even higher than 50%) are usually photoinactive, which bring light shielding effect to decrease the effective light absorption of loaded QDs, severely impeding their catalytic performance of QDs/graphene hybrids. To surmount above drawback, 2D $\text{g-C}_3\text{N}_4$ NSs (CNNSs), a promising visible light responsive material, is used as surface platform to prepare 0D/2D hybrids [24]. For instance, Ye and co-workers incorporated vanadate QDs onto CNNSs, which showed superior photocatalytic performance toward methyl orange due to the strong coupling and band alignment between them [16]. Zhang et al. prepared Co_3O_4 QDs/CNNSs hybrid to degrade tetracycline by activating peroxymonosulfate [17]. Co_3O_4 QDs (≈ 2.2 – 3.2 nm) were attached on $\text{g-C}_3\text{N}_4$ nanosheets, which exhibited improved synergistic effect of photo- and chemical catalytic performance and $\approx 98.7\%$ TC (50 mL, 0.5 g L^{-1}) was degraded under visible light irradiation for 60 min. However, it is worth noting that these reports mainly provide the construction of single-species QDs coupled NSs, making most 0D/2D composites fail to reach expected catalytic performance as heterogeneous catalysts. Therefore, the development of effective 0D/2D hybrids with multi-active sites that can combine unique advantages of QDs with the synergy of multi-active sites is highly desired, but is rarely reported to date.

Based on the above considerations, herein, a novel 0D/2D hybrid of bimetallic oxide QDs/CNNSs was fabricated through coupling Cu and Fe bi-metal oxide (CuFeO) QDs with ultrathin CNNSs via a facile one-step chemical reaction, followed by low-temperature annealing in air. The ultrafine CuFeO QDs (≈ 2 nm) were uniformly and firmly anchored on CNNSs, which not only provided more available surface active sites, but also expedited dramatically charge mobility. CuFeO QDs/CNNSs hybrid showed remarkable catalytic activity and stability towards TC degradation in the presence of H_2O_2 under visible light irradiation. The effects of Cu-Fe sites on CNNSs on charge separation and transfer, H_2O_2 activation and TC absorption were systematically investigated. More importantly, except for the enhanced charge separation and transfer, aiming at the uncertainty of the synergies of Cu-Fe sites towards Fenton reaction, H_2O_2 adsorption-activation trade-off on Cu-Fe sites was revealed in depth based on the DFT calculations. Multiple synergies of TC adsorption-catalytic degradation and photocatalysis-Fenton oxidation derived from the combined effect of Cu-Fe sites were clearly demonstrated, which could achieve a significant improvement in pollutant removal efficiency. In addition, a plausible synergetic degradation mechanism was also proposed. This work provides a new insight in developing multi-functional 0D/2D hybrids for a large variety of optoelectronic applications, not limited to photo-induced AOPs catalysis.

2. Experiment section

2.1. Preparation of ultrathin CNNSs

The ultrathin CNNSs were synthesized according to a two-step thermal polymerization [17]. In brief, a certain amount of urea was added to a crucible with a cover, then heated to 550°C ($2.5^\circ\text{C min}^{-1}$) for 4 h. The obtained yellow product was further heated to 500°C (5°C min^{-1}) for 2 h in an open crucible. Finally, light yellow CNNSs were obtained for later use.

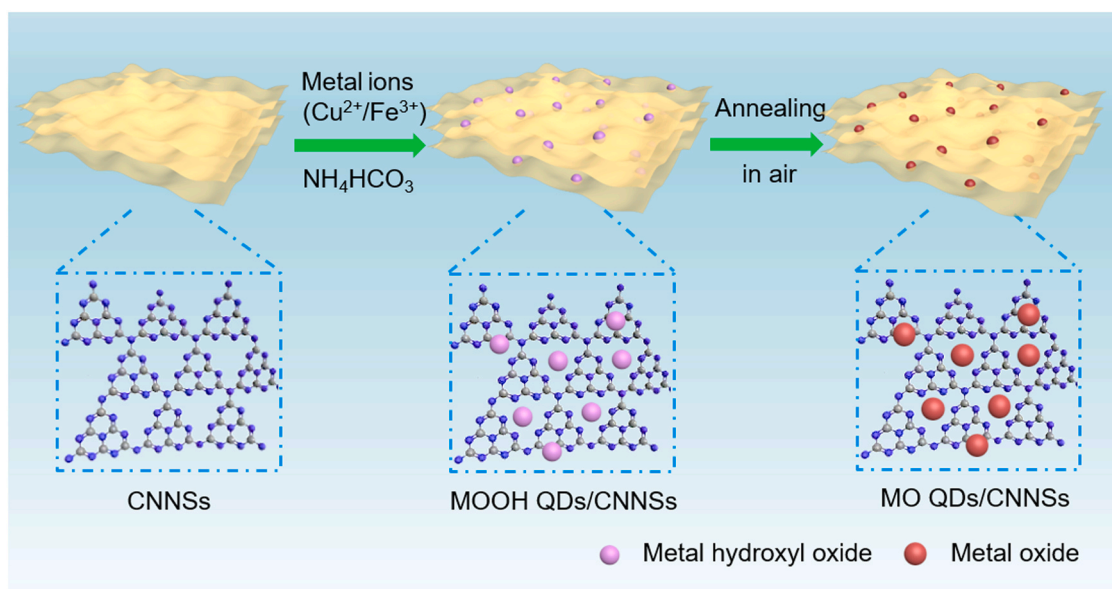
2.2. Preparation of CuFeO QDs/CNNSs hybrids

The CuFeO QDs/CNNSs hybrids were synthesized by one-step chemical reaction and low-temperature calcination [19,25]. In a typical synthesis procedure, 900 mg CNNSs was first dispersed in absolute ethanol (90 mL) with the assistance of sonication for 1.5 h. Then, 0.7 mmol of $\text{CuCl}_2 \cdot 2\text{H}_2\text{O}$ and 0.3 mmol of $\text{FeCl}_3 \cdot 6\text{H}_2\text{O}$ were dissolved in the above CNNSs suspension. After that, 3 mmol of NH_4HCO_3 was added with continuous stirring for 8 h at room temperature. The as-obtained MOOH QDs/CNNSs ($\text{M} = \text{Cu}$ and Fe) precursor was collected by centrifugation, washed several times with ethanol and distilled water, and dried at 40°C overnight in an oven. Finally, the precursor was heated to 350°C for 2 h in air with a rate of 5°C min^{-1} to obtain CuFeO (7:3) QDs/CNNSs hybrid (774 mg, greenish brown, Fig. S1). CuFeO QDs-x/CNNSs hybrids with other Cu:Fe molar ratios ($x = 9:1$, $5:5$ and $3:7$) were synthesized similarly through fixed 1 mmol of total metal precursor. For comparison, the individual Cu_xO QDs/CNNSs and Fe_2O_3 QDs/CNNSs were prepared using the same procedure, where 1 mmol $\text{CuCl}_2 \cdot 2\text{H}_2\text{O}$ and 1 mmol $\text{FeCl}_3 \cdot 6\text{H}_2\text{O}$ were added into the starting solution, respectively. Except otherwise noted, the CuFeO QDs/CNNSs sample discussed below was prepared with Cu:Fe raw ratio of 7:3.

2.3. Materials characterization

The crystal structures of the materials were determined by X-ray diffraction (XRD) with a Bruker D8 ADVANCE diffractometer (Cu K α irradiation, $\lambda = 1.5406 \text{ \AA}$). The surface morphology and fine structures were observed by field-emission scanning electron microscope (FE-SEM, Gemini SEM 300) and transmission electron microscope (TEM, Titan G260–300). The X-ray photoelectron spectroscopy (XPS) signals were obtained by a thermo K-Alpha spectrometer with an Al K α X-ray source (1486.6 eV). The binding energy was calibrated using the C1s level at 284.6 eV as an internal standard. Photoluminescence (PL) spectra was evaluated using a Hitachi F-7000 spectrometer under the 320 nm of excitation wavelength. Time-resolved PL spectra of the materials was recorded on a S4 pioneer spectrometer (Bruker AXS GmbH). The UV–vis diffuse reflectance spectroscopy (UV–vis DRS) was performed with a Lambda 950 spectrophotometer in the region of 200–800 nm with BaSO_4 as reflectance standard. The metal content of hybrids was tested by an inductively coupled plasma optical emission spectrometer (ICP-OES, Shimadzu ICPE-9000). The total organic carbon (TOC) was tested using a Shimadzu TOC-LCPN analyzer.

Photoelectrochemical properties were measured with a standard three-electrode configuration. Catalyst-loaded ITO electrode worked as working electrode, Ag/AgCl electrode as the reference electrode, and Pt foil as the counter electrode. Electrochemical impedance spectroscopy (EIS) was performed on Autolab PGSTAT 302 (Metrohm, Switzerland) over a frequency range from 0.1 Hz to 1 MHz at open-circuit potential in 0.1 M Na_2SO_4 solution containing 0.1 M H_2O_2 under a 410 nm light emitting diode (LED) light source. The introducing intensity-modulated photocurrent spectroscopy (IMPS) was carried out on Autolab PGSTAT 302 with the light source of a LED array (410 nm).



Scheme 1. Schematic illustration for the formation of CuFeO QDs/CNNs hybrid.

2.4. Adsorption tests of TC

The adsorption behaviors of the samples towards tetracycline (TC) were conducted in a glass reactor in the dark [26]. Briefly, 20 mg of different samples were respectively added into TC aqueous solution (40 mL, 50 mg/L) and stirred at room temperature. Samples were drawn every 5 min until equilibrium was reached, simultaneously analyzed the residual concentration of TC by recording the absorption peak at 357 nm using a UV-vis spectrophotometer.

2.5. Catalytic tests of photo-Fenton activation

The catalytic performance of CuFeO QDs/CNNs hybrids was evaluated based on the TC degradation in the presence of H_2O_2 under visible light irradiation. The catalytic reactions were performed in a jacketed beaker with condensed water under stirring. The light source was a 300 W of Xenon lamp equipped with wavelength cutoff filters ($\lambda \geq 420$ nm). The pH values of solution were adjusted using HCl or NaOH solution. In a typical experiment, 20 mg of catalyst was ultrasonically dispersed into TC solution (40 mL, 50 mg/L). 0.5 g L^{-1} was selected as catalyst dosage based on our previous report [2]. Before irradiation, the suspension was stirred in dark for 60 min to achieve an adsorptive-desorption equilibrium between catalyst and TC contaminant. Then, a certain amount of H_2O_2 (30 wt%) was added into the solution together with turning on the Xenon lamp. The light-induced Fenton reaction was started. At fixed time intervals during the degradation process, 3 mL of suspension was taken out and immediately separated by filtration through a $0.22 \mu\text{m}$ Millipore filter to remove the catalyst. The residual concentration of TC was analyzed using a UV-vis spectrophotometer. To evaluate the stability of catalyst, after each reaction, the solid catalyst was collected, washed, and dried to be reused in next cycle.

The active species generated in CuFeO QDs/CNNs- H_2O_2 /visible light system were investigated by trapping experiments, which were carried out in a similar experiment device as the TC catalytic degradation. Different scavengers, such as tertbutyl alcohol (TBA, 150 mM), 1,4-benzoquinone (BQ, 1 mM), ammonium oxalate (AO, 10 mM), silver nitrate (AgNO_3 , 10 mM) and furfuryl alcohol (FFA, 150 mM), were added into the TC pollution solution to trap hydroxyl radicals ($\cdot\text{OH}$), superoxide free radical ($\text{O}_2^{\cdot-}$), holes (h^+), electrons (e^-) and singlet oxygen ($^1\text{O}_2$), respectively. The generated $\cdot\text{OH}$ and $\text{O}_2^{\cdot-}$ were further detected with the trapping agent of 5,5-dimethyl-1-pyrroline-N-oxide

(DMPO, 0.2 M) on a Bruker micro ESR spectrometer, while 2,2,6,6-tetramethyl-4-piperidinol (TEMP, 0.2 M) was used as the spin-trapping agent for $^1\text{O}_2$. The operating parameters of EPR were provided as below: microwave power = 10.0 mW, center field = 3514.7 G, sweep width = 100 G, sweep time = 5.7 s, and scan number = 50.

3. Results and discussion

3.1. Synthesis and characterization of CuFeO QDs/CNNs hybrid

The CuFeO QDs/CNNs hybrid was prepared by a facile one-step chemical reaction and subsequently low-temperature annealing treatment. The detailed synthesis process and formation mechanism were shown in Scheme 1. The CNNs were dispersed in ethanol solution, in which highly dispersed CuFeO QDs were in situ formed on the surface of CNNs by adding CuCl_2 , FeCl_3 and NH_4HCO_3 under stirring, followed by a low-temperature calcination in air. As shown in Fig. S2, the zeta potential of CNNs was -17.2 mV , which could easily adsorb positively charged Cu^{2+} and Fe^{3+} ions through electrostatic interaction. Furthermore, substantial nitrogen atoms containing lone-pairs of electron in the plane of CNNs were generally ideal sites for anchoring metal ions, which could inhibit significantly the agglomeration of metal species [16]. Subsequently, amorphous MOOH ($\text{M} = \text{Cu}$ and Fe) QDs were in situ preliminarily formed by adding NH_4HCO_3 based on the following chemical reaction $\text{MCl}_x + \text{NH}_4\text{HCO}_3 \rightarrow \text{MOOH} + \text{CO}_2 + \text{H}_2\text{O} + \text{NH}_4\text{Cl}$. After low-temperature calcination, uniform CuFeO QDs with ultrasmall sizes and clear lattice fringes were obtained on CNNs. The formation of uniform and ultrafine CuFeO QDs on CNNs surface was mainly due to the homogeneous reaction and N-binding effect of CNNs. This method is simple, economic and scalable for the preparation of 0D metal oxide-based nanocomposites with polymetallic sites.

The crystal structure and phase compositions of pristine CNNs and 0D/2D hybrids were confirmed by XRD patterns. As shown in Fig. S3, for pristine CNNs, the characteristic peak at 13.0° was ascribed to the (100) plane due to the in-plane structure of nitrogen-linked heterocyclic rings and the strong peak at 27.7° was well indexed to (002) plane, corresponding to the stacking of conjugated aromatic systems [27–31]. However, the absence of the diffraction peaks of metal oxide for all the 0D/2D hybrids might be attributed to their low loading and high dispersion degree. To further verify the crystal structure of metal oxides, the synchrotron-based high energy X-ray diffraction (HE-XRD) was

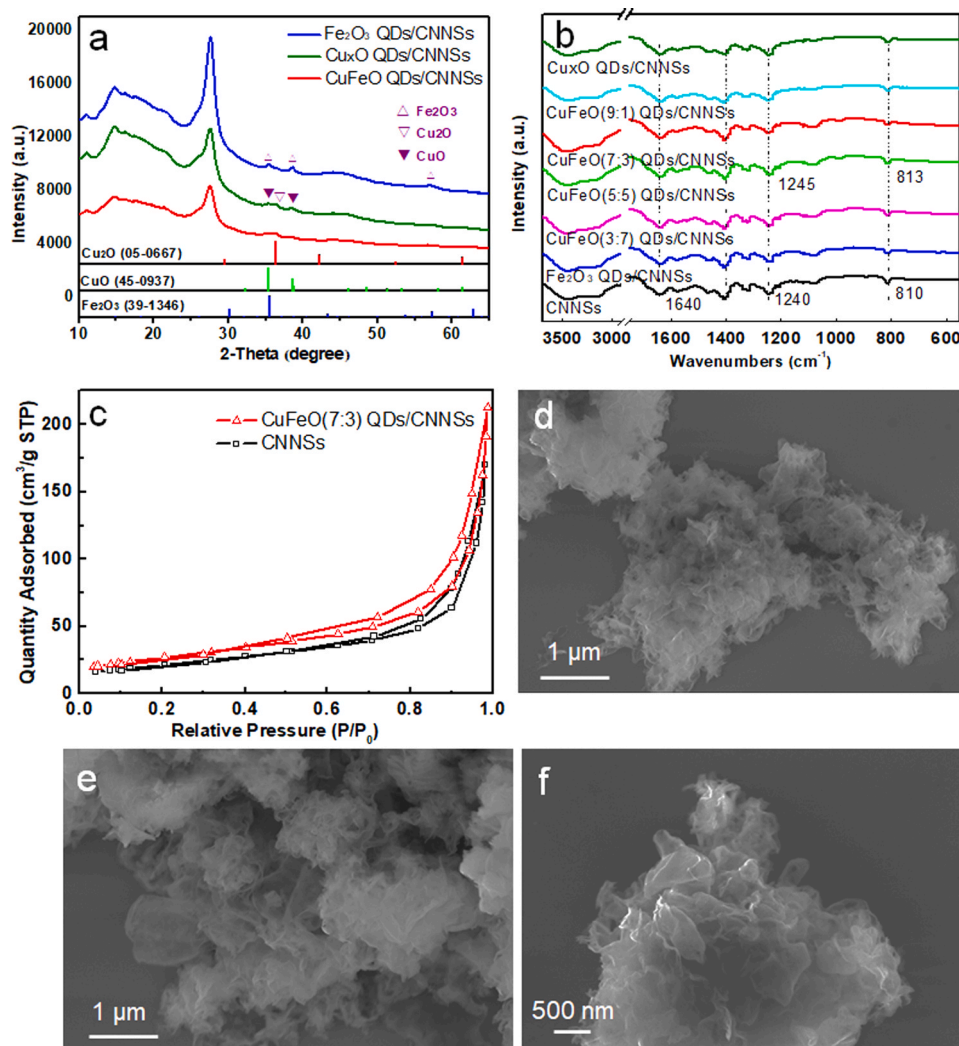


Fig. 1. (a) Synchrotron-based high energy XRD patterns, (b) FT-IR spectra, (c) N₂ adsorption-desorption isotherms of pure CNNSs and QDs loaded CNNSs composites, SEM images of (d) CNNSs and (e, f) CuFeO QDs/CNNSs hybrid.

carried out (Fig. 1a). For sample prepared using Fe precursor (Fe₂O₃ QDs/CNNSs), three diffraction peaks at 35.6°, 38.7° and 57.2° were observed, corresponding to the (311), (320) and (511) crystal plane of Fe₂O₃ (JCPDS No. 39-1346). For the sample prepared using Cu precursor (Cu_xO QDs/CNNSs), the peaks at 35.6° and 38.7° were belonged to the (002) and (111) planes of CuO (JCPDS No. 45-0937), while the diffraction peak at 36.4° was assigned to the (111) plane of Cu₂O (JCPDS No. 05-0667). The results indicated that the copper oxide was a Cu₂O-CuO hybrid [32,33]. For CuFeO QDs/CNNSs hybrid, no new peaks were observed except for the characteristic peaks of Fe₂O₃, Cu₂O and CuO, demonstrating the successful coupling of Cu-Fe bimetallic oxide with CNNSs. In addition, all samples showed two diffraction peaks at 27.7° and 13.0°, indicating that QDs did not cause a change in the crystal structure of CNNSs. FT-IR spectra was used to reveal the chemical structure of CuFeO QDs/CNNSs hybrids, which was displayed in Fig. 1b. As for CNNSs, the bands located at 3440 and 3140 cm⁻¹ belonged to the stretch of O-H and N-H components. The peaks at about 1640–1240 cm⁻¹ corresponded to C-N stretching, stretching vibration modes of C-N heterocyclic ring and stretching vibration of C-NH-C connected units, respectively. The absorption band observed at ≈ 810 cm⁻¹ represented the characteristic s-triazine unit mode [34]. For Cu_xO QDs/CNNSs, Fe₂O₃ QDs/CNNSs and CuFeO QDs/CNNSs composites, the characteristic bands of CNNSs could be clearly observed, indicating that the loading of metal oxide QDs did not change the

chemical structure of CNNSs. This observation was consistent with the results obtained from XRD patterns. Interestingly, there was a slight shift in characteristic peak positions of CuFeO QDs/CNNSs compared with pristine CNNSs, suggesting strong interactions between CuFeO QDs and CNNSs in hybrids. It is favorable for improving the interfacial transfer of photogenerated charges from CNNSs to CuFeO QDs, increasing the chances of charge participating in AOPs, and improving photogenerated charges separation. Thus, photo-Fenton catalytic activities could be enhanced. The specific surface area and pore structure of pristine CNNS and CuFeO QDs/CNNSs were analyzed by N₂ adsorption-desorption characterization (Fig. 1c). In contrast, the surface area of CuFeO QDs/CNNSs was 95.11 m² g⁻¹, which was higher than that of CNNSs. This might be attributed to better layers separation of CNNSs caused by the insertion of CuFeO QD. The pore volume of CNNS and CuFeO QDs/CNNSs were about 0.26 and 0.32 cm³ g⁻¹, respectively (Table S1). The pore sizes of these two samples were in a wide range of 3.5–20 nm (Fig. S4), implying the presence of mesopores structure [35]. High surface area could provide more surface active sites, and porous structure could facilitate the diffusion of H₂O₂ and pollutants to improve the reaction kinetics. The above two features could synergistically promote catalytic performance of CuFeO QDs/CNNSs hybrid.

To further investigate the morphology and microstructure of CuFeO QDs/CNNSs hybrid, FE-SEM and TEM were performed. As displayed in Fig. 1d and e, CNNSs and CuFeO QDs/CNNSs showed similar

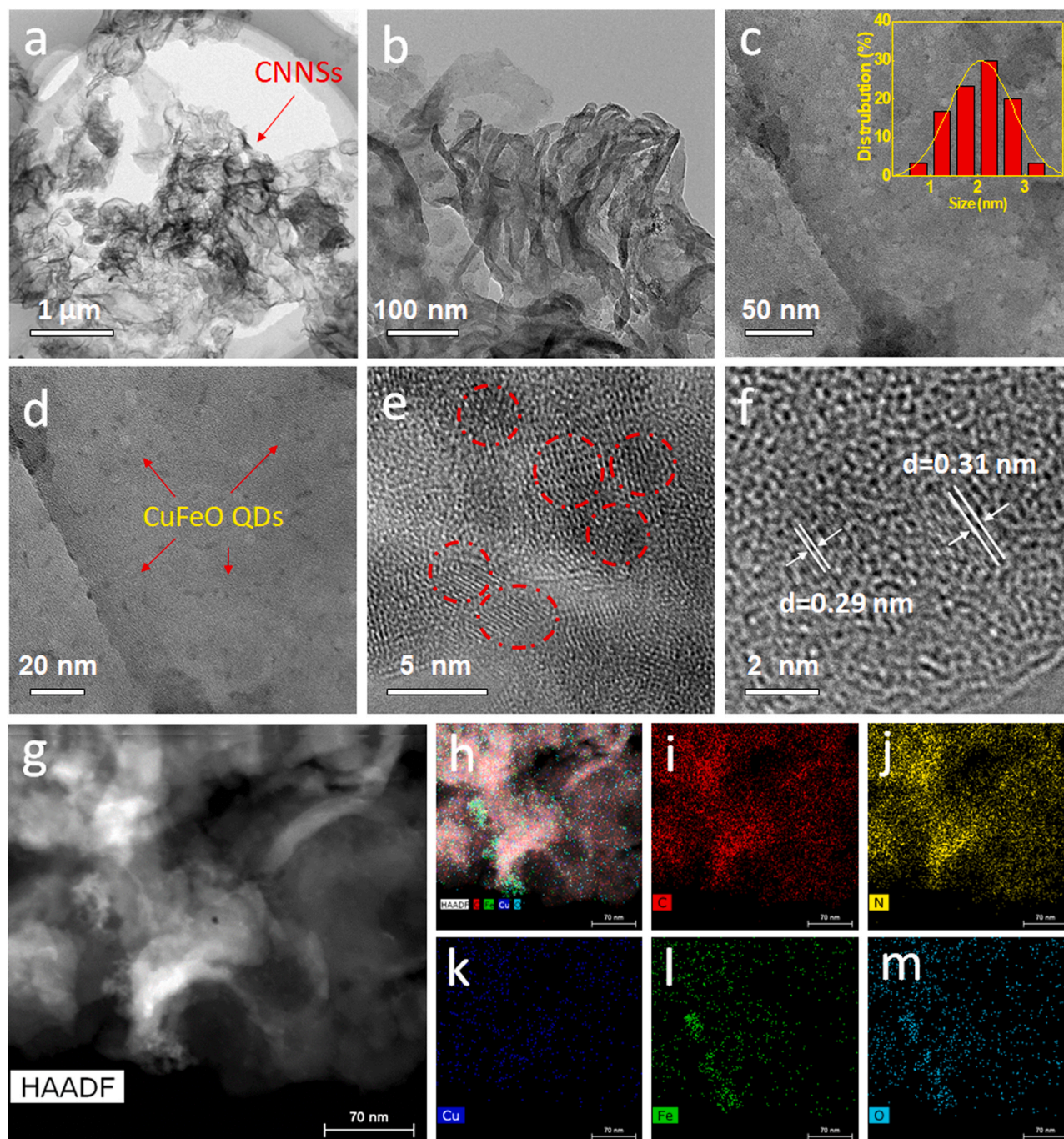


Fig. 2. (a-c) TEM and (d-f) HR-TEM images of CuFeO QDs/CNNs hybrid; (g-m) STEM image and the corresponding elemental mapping images of CuFeO QDs/CNNs hybrid.

hierarchical morphology comprising of a large number of crumpled nanosheets with wrinkles and folds. The magnified SEM image further verified the ultrathin features of these nanosheets (Fig. 1f). 2D ultrathin nanosheets can provide sufficient surface reaction sites and accelerate charge separation by shortening charge diffusion length. Notably, CuFeO nanoparticles could not be observed on CNNs surface in FE-SEM images because of their ultrafine particle size. As shown in Fig. 2a and b, TEM images also revealed the wrinkled morphology of CuFeO QDs/CNNs. In high-magnification TEM images of CuFeO QDs/CNNs (Fig. 2c-d), abundant in-plane holes with a few nanometer diameter and homogeneously dispersed bimetallic oxide nanocrystallines (1.0–3.5 nm) could be clearly observed on the surface of interconnected ultrathin CNNs, demonstrating holey structured CNNs thin sheets and

uniform loading of ultra-small nanoparticles. Moreover, no isolated CuFeO QDs could be observed, which indicated that CNNs could closely anchor CuFeO QDs and effectively prevent them from agglomeration. Seen from high-resolution TEM (HRTEM, Fig. 2e-f) images, the particle sizes of anchored CuFeO QDs were centered at $\approx 2-3$ nm, which was in keeping with the statistical particle size distribution diagram (Insert of the Fig. 2c). The lattice spacing of 0.29 nm and 0.31 nm were matched well with (220) plane in the Fe_2O_3 lattice and (110) plane in the Cu_2O lattice, respectively [32]. The Cu_2O and Fe_2O_3 crystal lattice intersected with each other in the particle area, indicating the coexistence of Cu and Fe oxides in nanocrystallines. HRTEM also showed the high crystallinity and ultrasmall nature of CuFeO QDs, which not only could expose more Cu-Fe synergistic sites but also could accelerate

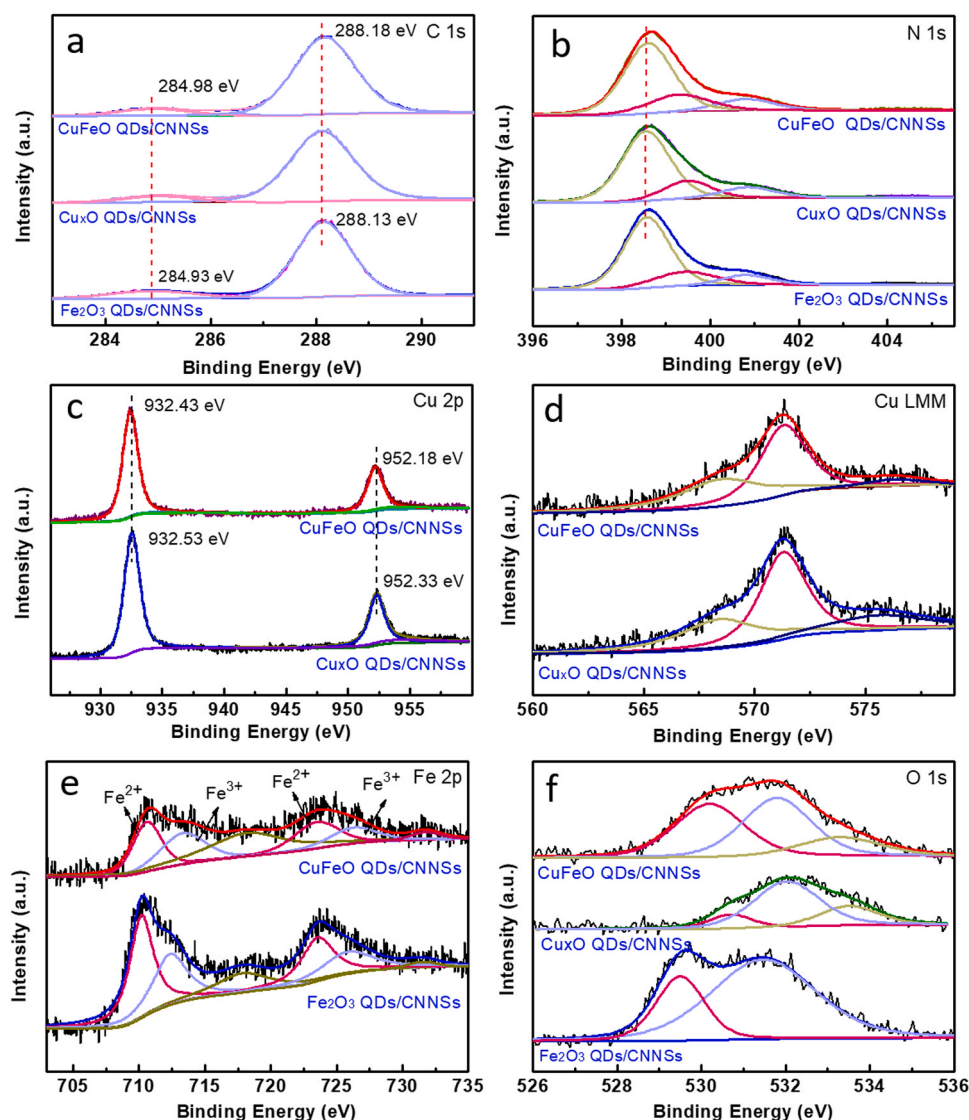


Fig. 3. XPS spectra of (a) C 1 s, (b) N 1 s, (c) Cu 2 p, (d) Cu LMM (e) Fe 2 p, and (f) O 1 s for Cu_xO QDs/CNNs, Fe_2O_3 QDs/CNNs and CuFeO QDs/CNNs hybrid.

electrons to diffuse toward the surface, thus significantly improved its Fenton catalytic activity. In addition, according to HAADF-STEM and corresponding elemental mapping images conducted for CuFeO QDs/CNNs (Fig. 2g-m), we unambiguously confirmed the presence of C, N, O, Fe and Cu elements in hybrid, wherein Fe, Cu and O elements were distributed evenly over the whole nanosheets. The above results demonstrated the in situ formation of CuFeO QDs with a uniform dispersion at micro level, thus leading to the formation of strongly coupled heterostructure hybrids.

The surface chemical states of CuFeO QDs/CNNs were further explored by XPS. As expected, the full scan spectrum demonstrated the existence of Cu, Fe and O in the hybrids along with C and N elements of CNNs (Fig. S5). As observed in Fig. 3a, high-resolution C 1 s spectrum could be deconvoluted into two peaks, including around 284.9 eV for graphitic carbon (C-C/C=C) and 288.1 eV for sp^2 -hybridized carbon in N-C=N triazine rings of CNNs, respectively [36]. However, the peaks of C 1 s signals shifted to higher binding energies after loading Fe_2O_3 QDs, Cu_xO QDs or CuFeO QDs (Fig. S5), indicating the electronic interaction between QDs and CNNs derived from orbital hybridizations between CNNs and Cu_2O - Fe_2O_3 . For the N 1 s spectrum of CuFeO QDs/CNNs (Fig. 3b), the peaks with binding energies of round 398.6, 399.4 and 400.8 eV were assigned to sp^2 -hybridized N (C-N=C) species, tertiary N (N-(C)₃) groups and amino functional (N-H) bonds,

respectively [14,37]. Obviously, the binding energy of sp^2 -hybridized N species of CuFeO QDs/CNNs was higher than that of Fe_2O_3 QDs/CNNs and Cu_xO QDs/CNNs systems, indicating the change of chemical environments after the formation of CuFeO QDs. This observation pointed to the synergistic effect of Cu_2O - Fe_2O_3 in composite material and also indicated that CuFeO/CNNs with multi-metal sites could accelerate the electron transfer from N sites in CNNs to metal oxides via orbital hybridizations between Cu_xO , Fe_2O_3 and CNNs, which increased the electron density of CuFeO QDs and was beneficial for participating in subsequent catalytic reactions. The Cu 2 p spectra was shown in Fig. 3c. The characteristic peak of Cu $2\text{p}_{3/2}$ at 932.4 eV and the peak of Cu $2\text{p}_{1/2}$ at 952.2 eV were attributed to the Cu^+ [38], implying that Cu_2O was the dominant Cu species. In Cu LMM spectrum (Fig. 3d), the main peak at 571.4 eV further confirmed the formation of Cu_2O . The weak peak at around 568.7 eV was identified as Cu metal [39]. Interestingly, an obvious shift of Cu 2 p peaks in CuFeO QDs/CNNs also was observed compared with that of Cu_xO QDs/CNNs (932.5 eV), indicating the strong electronic interaction between Fe, Cu and CNNs components. When coupled with Fe_2O_3 QDs, Cu species gained more electrons, revealing the electrons transfer from CNNs and Fe species to Cu species. For Fe 2 p spectrum of CuFeO QDs/CNNs (Fig. 3e), the peaks at 710.7 and 723.8 eV were assigned to Fe^{2+} species, the weaker peaks at 713.5 and 726.5 eV were ascribed to Fe^{3+} species, and the peaks at 718.5 and

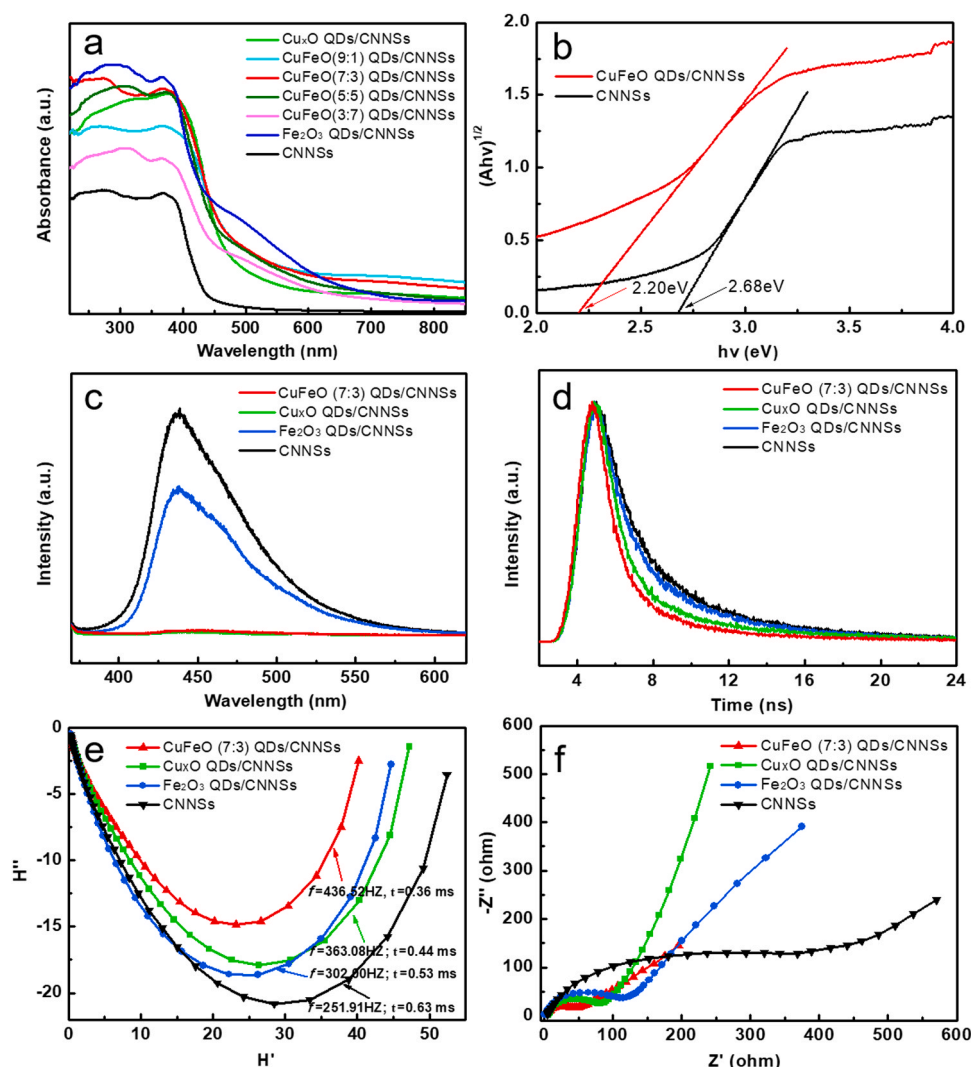


Fig. 4. (a) UV-vis DRS, (b) the bandgap values estimated by a related curve of $(A\lambda)^{1/2}$ versus $h\nu$ plotted, (c) PL emission spectra (excitation wavelength is 395 nm), (d) time-resolved PL decay curves of the different samples; (e) IMPS and (f) EIS Nyquist plots of the catalysts measured in 0.1 M Na₂SO₄ solution containing 0.1 M H₂O₂ with light irradiation.

731.8 eV belonged to satellite peaks, which implied the formation of iron oxide and also confirmed the coexistence of Fe²⁺ and Fe³⁺ in CuFeO QDs/CNNs hybrid [40]. Moreover, the peak position of Fe 2p in CuFeO QDs/CNNs hybrid shifted to higher binding energies in comparison with that of Fe₂O₃ QDs/CNNs, suggesting the electron transfer from Fe species to other components. This observation was in accord with the results of N 1 s spectrum (Fig. 3b) and Cu 2p spectrum (Fig. 3c). As for O 1 s spectrum (Fig. 3f), the peaks centered at about 530.2, 531.8 and 533.3 eV could be ascribed to lattice oxygen (O²⁻) due to oxygen atoms bound to metals, defect sites with low oxygen coordination and absorbed oxygen or H₂O, respectively [12]. Compared with Cu_xO QDs/CNNs, the intensified peaks at 531.8 eV in CuFeO QDs/CNNs should be responsible for the existence of more oxygen vacancies than Cu_xO QDs/CNNs by introducing Fe species. This would enhance the overall catalytic activities of CuFeO QDs/CNNs via increasing substrate trapping (i.e. photoinduced electrons and H₂O₂) and prolonging lifetime of reducing equivalents [41], which could not only improve charge separation efficiency, but also promote effective contact between catalyst and H₂O₂ in Fenton reaction. All these results of XPS spectra illustrated the intimate interaction between metal oxide QDs and CNNs, and the electronic synergy between Cu species and Fe species, which could collectively facilitate the catalytic processes in photo-Fenton reactions.

3.2. Optical and photoelectric properties of CuFeO-x QDs/CNNs hybrid

To investigate the optical property of the hybrids, UV-vis DRS was performed (Fig. 4a). The wavelength of CNNs adsorption edge was located at 427 nm, which was in accordance with a band gap of 2.68 eV for CNNs [42]. After coupling of Fe₂O₃ QDs or Cu_xO QDs, they showed an enhanced absorption in visible light owing to the grafting of Fe or Cu species as visible-light absorbers, and the bandgaps decreased to 2.01 eV and 2.38 eV, respectively (Fig. S6) [20]. When Fe₂O₃-Cu_xO were simultaneously introduced into CNNs, the hybrid extended the absorption range covering the whole visible light region and showed a narrow bandgap of 2.20 eV (Fig. 4b). In addition, Cu_xO was a p-type semiconductor, while CNNs and Fe₂O₃ were n-type, which could form a steady p-n junction. Therefore, the CuFeO QDs/CNNs exhibited a more outstanding optical property.

PL spectra and photoelectrochemical measurements were applied to explore the separation and migration of photogenerated charge. As presented in Fig. 4c, after loading metal oxide QDs, especially Cu_xO QDs, the emission intensity dramatically decreased in contrast with that of pristine CNNs. CuFeO QDs/CNNs exhibited similar emission intensity with Cu_xO QDs/CNNs, demonstrating a fact that the coexistence of Fe₂O₃ QDs and Cu_xO QDs could greatly suppress charge recombination and facilitate interfacial charge transfer. Photocurrent responses in dark

Table 1The values estimated PL lifetime τ_i and corresponding constant A_i .

Sample	τ_1 (ns)	A_1	τ_2 (ns)	A_2	τ_3 (ns)	A_3	$\langle\tau\rangle$ (ns)
CNNs	1.13	2813.59	4.27	539.40	26.58	40.48	6.41
Fe ₂ O ₃ QDs/ CNNs	1.58	2186.90	4.84	977.60	19.25	86.50	6.13
Cu _x O QDs/ CNNs	2.08	2495.70	7.50	661.50	–	–	4.73
CuFeO QDs/ CNNs	1.20	2599.0	5.97	539.20	–	–	3.62

and light conditions were carried out to probe the efficiency of charge transfer. As shown in Fig. S7, after loading Fe₂O₃ and Cu_xO QDs, photocurrent intensity remarkably increased compared with CNNs. Cu_xO QDs/CNNs showed the highest photocurrent intensity, which was slightly higher than CuFeO QDs/CNNs. This phenomenon was consistent with the results of PL spectra, which indicated that CuFeO QDs not only could boost the charge separation but also could accelerate release and transfer them. The emission lifetime was analyzed by time-resolved PL decay spectra. The catalysts exhibited exponential decay with fast components (Fig. 4d). Decay times (τ_1 , τ_2 , τ_3), PL aptitudes (A_1 , A_2 , A_3) and the intensity-average lifetime ($\langle\tau\rangle$) were listed in Table 1. The $\langle\tau\rangle$ was calculated through the following equation:

$$\langle\tau\rangle = \frac{A_1\tau_1^2 + A_2\tau_2^2 + A_3\tau_3^2}{A_1\tau_1 + A_2\tau_2 + A_3\tau_3} \quad (1)$$

The $\langle\tau\rangle$ values of CNNs, Fe₂O₃ QDs/CNNs, Cu_xO QDs/CNNs and

CuFeO QDs/CNNs were deduced to be 6.41 ns, 6.13 ns, 4.73 ns and 3.62 ns, respectively. CuFeO QDs/CNNs exhibited the shortest average lifetime, indicating the best charge transfer and separation. The emission quenching accompanied with a notable decrease of the emission lifetime in CuFeO QDs/CNNs implied a non-radiative pathway from the electronic interaction between CNNs and CuFeO QDs [16]. In addition, the electron-transfer rate constant (k_{et}) of CuFeO QDs/CNNs was calculated to be $1.20 \times 10^8 \text{ s}^{-1}$ using the Eq. (2):

$$k_{et}(\text{CNNs} \rightarrow \text{CuFeOQDs}) / \text{CNNs} = \frac{1}{\langle\tau\rangle(\text{CuFeOQDs/CNNs})} - \frac{1}{\langle\tau\rangle(\text{CNNs})} \quad (2)$$

The charge transfer dynamics were analyzed by IMPS. The average transport times (τ) of photoexcited electrons diffused to the electrode could be calculated by the equation ($\tau_D = (2\pi f_{\text{IMPS}})^{-1}$), where f_{IMPS} is the frequency at which the minimum in the IMPS plot occurs. The transport times (τ) for pristine CNNs, Fe₂O₃ QDs/CNNs, Cu_xO QDs/CNNs and CuFeO QDs/CNNs were calculated to be 0.63, 0.53, 0.44 and 0.36 ms, respectively (Fig. 4e). Among them, CuFeO QDs/CNNs displayed the shortest transport time, which indicated that the charge transfer was much faster and easier at the interfaces of CNNs and CuFeO QDs. Furthermore, we found that the recombination sites in CuFeO QDs/CNNs were fewer due to the strong coupling between CNNs and CuFeO QDs as well as synergistic effect of Fe₂O₃ and Cu_xO that was confirmed by XPS. The charge transfer kinetics at interfaces between solid catalysts and reaction solution containing H₂O₂ was evaluated by

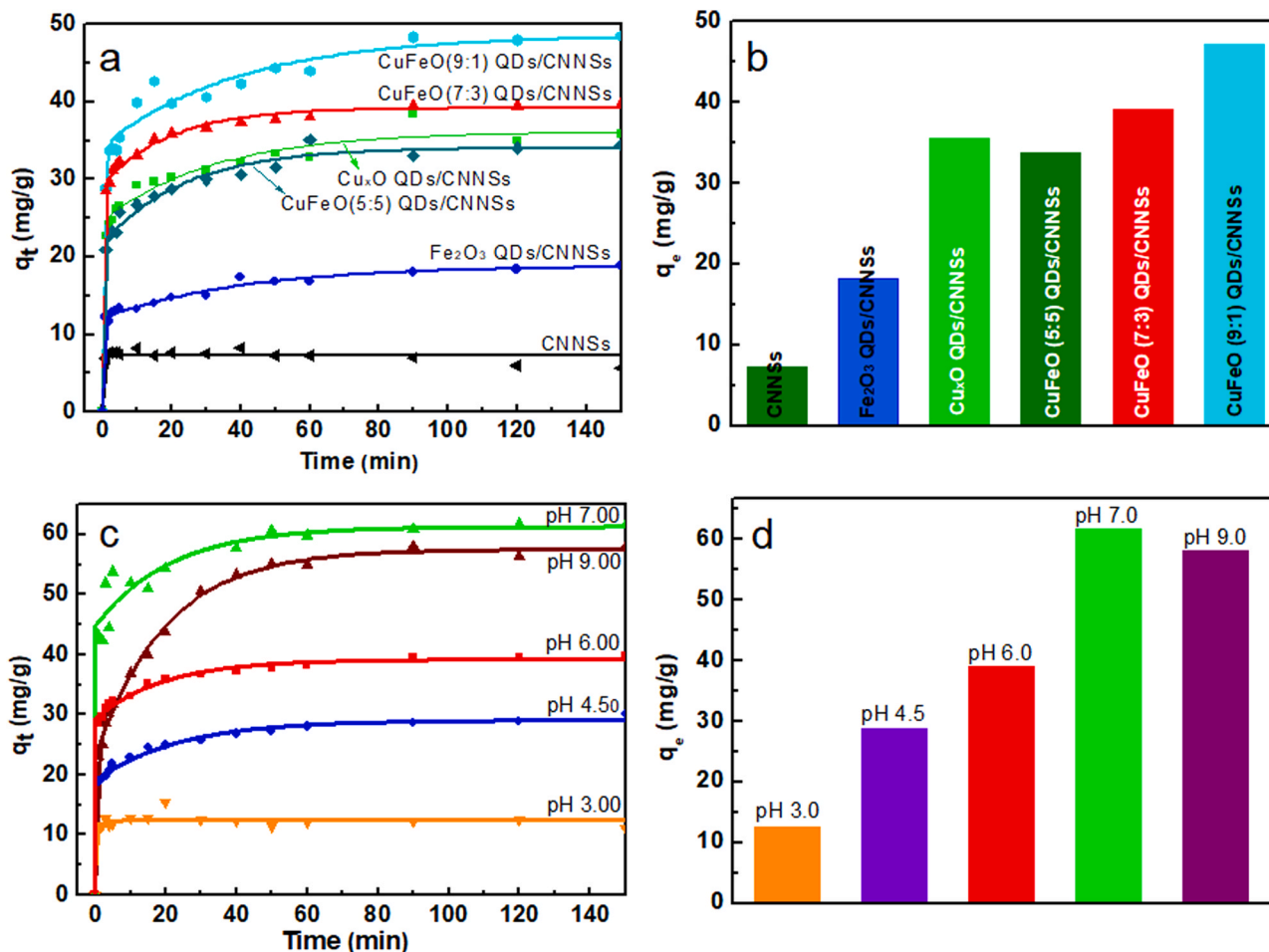


Fig. 5. (a) TC (50 mg/L) adsorption on different samples at pH = 6, (b) the corresponding equilibrium TC adsorption capacities, (c) TC absorption at different pH values on CuFeO QDs/CNNs and (d) the corresponding equilibrium TC adsorption capacities.

EIS. The smaller semicircle in the Nyquist plots presented smaller electrical resistance for surface charge transfer and higher charge transfer efficiency [43]. As reflected by impedance arc radius in Fig. 4f, CuFeO QDs/CNNs exhibited the smallest electrical resistance compared with that of CNNs, Fe₂O₃ QDs/CNNs or Cu_xO QDs/CNNs under visible-light irradiation in H₂O₂ solution, implying a faster interfacial reaction benefiting from the improved interfacial charge separation and the incremental activation of H₂O₂ through the synergy of Fe and Cu sites.

3.3. Adsorption behavior of TC on CuFeO-x QDs/CNNs hybrids

Better adsorption of pollutants onto the catalysts is a critical factor for the effective photo-Fenton degradation. Fig. 5a illustrated the adsorption capacities of different catalysts with respect to TC. All the supported catalysts absorbed TC rapidly within 3 min, subsequently the adsorption rates gradually declined and the saturation adsorption was reached at 90 min. As shown in Fig. 5b, CNNs showed an equilibrium adsorption of 7.30 mg/g towards TC. The π - π conjugation between CNNs and benzene rings in TC molecules and the presence of abundant in-plane holes in CNNs enabled fast TC transport to CNNs, achieving strong and rapid TC adsorption on the surface of CNNs. Meanwhile, TC adsorption capacities equaled to 18.11 and 35.52 mg/g for Fe₂O₃ QDs/CNNs and Cu_xO QDs/CNNs, respectively, suggesting that introducing Fe and Cu species could dramatically improve the TC adsorption by complexing action between surface Cu/Fe sites and amine groups of TC molecules as well as the strong affinity of the oxygen-containing functional groups (C=O, -OH) on TC molecules towards Cu/Fe sites. TC adsorption capacities of CuFeO (5:5) QDs/CNNs, CuFeO (7:3) QDs/CNNs and CuFeO (9:1) QDs/CNNs reached 33.79, 39.10 and 47.17 mg/g, respectively. To a certain extent, the amounts of adsorbed TC increased with the increase of Cu/Fe ratios. Excitingly, CuFeO QDs/CNNs showed better adsorption capability towards TC in contrast with Fe₂O₃ QDs/CNNs or Cu_xO QDs/CNNs. This excellent adsorption ability of CuFeO QDs/CNNs might be ascribed to the following two reasons. On the one hand, bi-metal oxide QDs were inserted in CNNs layers, which resulted in different degrees of tearing between CNNs membranes, and thereby provided more adsorption sites [44]. This phenomenon also was proved by the incremental specific surface area (75.03 m² g⁻¹ to 95.11 m² g⁻¹; Table S1). On the other hand, electron transfer between CuFeO QDs and CNNs derived from the synergy of Fe₂O₃ and Cu_xO QDs promoted the coordination ability of Cu-Fe sites on CNNs, which was beneficial for TC adsorption. In addition, as illustrated in Fig. 5c and d, TC adsorption capacity of CuFeO QDs/CNNs depended on pH values of the solution to a large extent. The adsorption capacity decreased from 39.10 mg/g at pH = 6.0–12.5 mg/g at pH = 3.0. This was due to that the amino groups and oxygen-containing groups in TC molecules were protonated below pH 5.5 and transformed into -NH₃⁺ and -OH₂⁺ [45], which reduced the coordination ability of TC with Cu-Fe species. It showed that the highest adsorption capacity (61.1 mg/g) were obtained at neutral condition. The superiority of CuFeO QDs/CNNs exhibiting outstanding TC adsorption capacities at high pH values was favorable for CuFeO QDs/CNNs to obtain excellent photo-Fenton activity in a wide pH working range.

The TC adsorption mechanism of CuFeO QDs/CNNs was investigated by using two common kinetic models, pseudo-first-order and pseudo-second-order kinetic models, which can be described by the following equations [44]:

$$\ln(q_e - q_t) = \ln q_e - k_1 t \quad (3)$$

$$\frac{t}{q_t} = \frac{1}{k_2 q_e^2} + \frac{t}{q_e} \quad (4)$$

Where q_e (mg/g) and q_t (mg/g) are the amount of TC adsorbed at equilibrium and at time t (min), k_1 (1/min) and k_2 (g/(mg min)) are the

Table 2

Kinetic parameters of TC adsorption on CuFeO QDs/CNNs at pH = 6.

q_e (exp)	pseudo-first-order			pseudo-second-order		
	k_1	q_e (cal)	R_1^2	k_2	q_e (cal)	R_2^2
39.10	0.65	36.54	0.68	0.054	37.87	0.97

pseudo-first-and pseudo-second-order rate constants, respectively. The obtained adsorption kinetics data and correlation coefficients (R^2) were summarized in Table 2. The pseudo-second-order kinetics model fitted well with the experimental results, exhibiting a linear regression coefficient (R_2^2) value (≈ 0.97) compared with R_1^2 value (≈ 0.68). π - π conjugation of CNNs and TC as well as complexing action between Cu-Fe sites and nitrogen/oxygen-containing groups contributed to fast and high adsorption of catalysts toward pollutants, which was a prerequisite for outstanding photo-Fenton catalysis.

3.4. Photo-Fenton catalytic performance for TC degradation

The catalytic performance was evaluated by the degradation of TC in the presence of H₂O₂ under visible light irradiation ($\lambda \geq 420$ nm) at room temperature. As shown in Fig. 6, hybrids with bimetallic oxide QDs showed enhanced catalytic efficiency towards TC degradation compared with single Fe₂O₃ or Cu_xO QDs coupled CNNs. The TC removal efficiency increased with molar ratios of Cu/Fe from 3:7–7:3, and further increasing the molar ratios of Cu/Fe to 9:1 did not cause significant improvement in the removal efficiency. CuFeO (7:3) QDs/CNNs hybrid exhibited the highest degradation efficiency of 99.8% (the average of three experiments, Fig. S8). TC mineralization ability was also investigated during degradation. As depicted in Fig. S9, the TOC removal ratio of CuFeO (7:3) QDs/CNNs, CuOx QDs/CNNs and Fe₂O₃ QDs/CNNs was 69.0%, 45.0% and 36.6%, respectively, indicating that higher mineralization ability was acquired by the synergy of Fe and Cu species. The CuFeO QDs/CNNs exhibited the high TOC removal efficiency, which ensured its practical application potentials. This increased catalytic activity was consistent with the advantages of optoelectronic and surface/interface properties of CuFeO QDs/CNNs as discussed above. To explore the catalytic process, control experiments were carried out under different conditions, as exhibited in Fig. 6b. It was found that TC was hardly removed by only irradiation or by H₂O₂ under light irradiation without catalysts, indicating weak direct photolysis of TC and H₂O₂. When CuFeO (7:3) QDs/CNNs was added to the system under visible light irradiation, TC photodegradation efficiency was dramatically enhanced. Noticeably, about 94.9% of TC was removed using CuFeO (7:3) QDs/CNNs in the presence of only H₂O₂, indicating the strong Fenton activity of the catalyst toward H₂O₂. $\approx 99.8\%$ of TC was decomposed by CuFeO (7:3) QDs/CNNs in the presence of H₂O₂ and visible light irradiation, suggesting that photocatalysis and Fenton catalysis had a synergistic effect in the removal of TC.

The effects of H₂O₂ dosage, TC concentration and initial pH on the degradation of TC by CuFeO QDs/CNNs were studied. As shown in Fig. 6c, the TC degradation rates were improved as H₂O₂ dosage increased from 0 mM to 100 mM. However, further increase of H₂O₂ dosage to 150 mM did not cause an improvement of degradation efficiency. As expected, increasing H₂O₂ dosage could produce more radical species, while overdose of H₂O₂ would consume the generated radical species ($\bullet\text{OH} + \text{H}_2\text{O}_2 \leftrightarrow \text{HO}_2\bullet + \text{H}_2\text{O}$). Fig. 6d showed the catalytic performance of CuFeO QDs/CNNs at different initial pH values. It showed highly effective for TC degradation in the pH range of 3.0–9.0. Notably, the catalytic activity kept almost unchanged even at pH = 9.0, which proved a wider pH working range than Fenton system (pH = 3–4). Large and fast TC absorption of CuFeO QDs/CNNs at high pH value also contributed to such good catalytic performance. In this work, the catalytic activity of all samples was evaluated at pH = 6.0 which was pristine pH of TC aqueous solution without any adjustment.

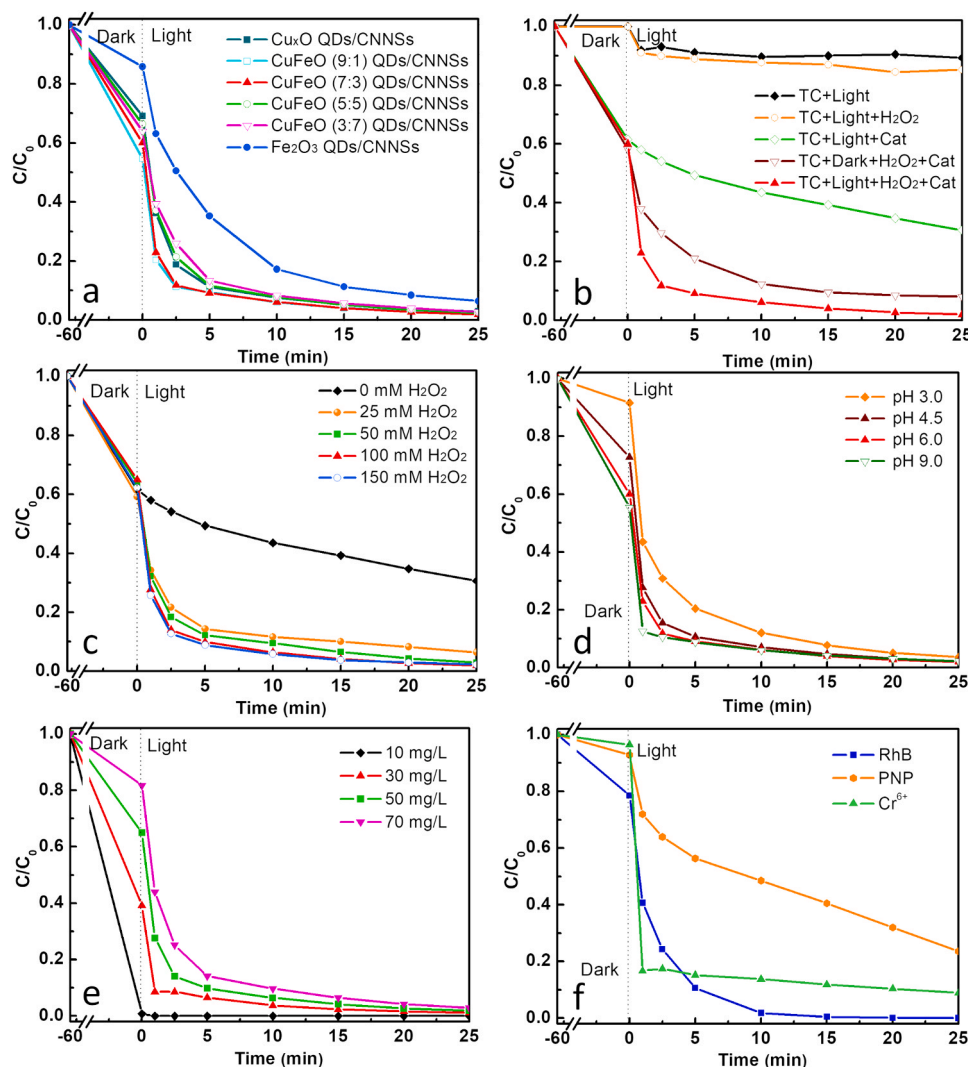


Fig. 6. The effects of (a) Cu/Fe ratios, (b) catalytic conditions, (c) H₂O₂ concentration, (d) initial pH values, and (e) TC concentration on the TC degradation by CuFeO (7:3) QDs/CNNSSs hybrid; (f) the degradation of different organic pollutants in CuFeO (7:3) QDs/CNNSSs-H₂O₂/vis systems. [Conditions: initial pH = 6.0; H₂O₂ = 100.0 mM; catalyst dosage = 0.5 g L⁻¹; pollutants = 50.0 mg/L].

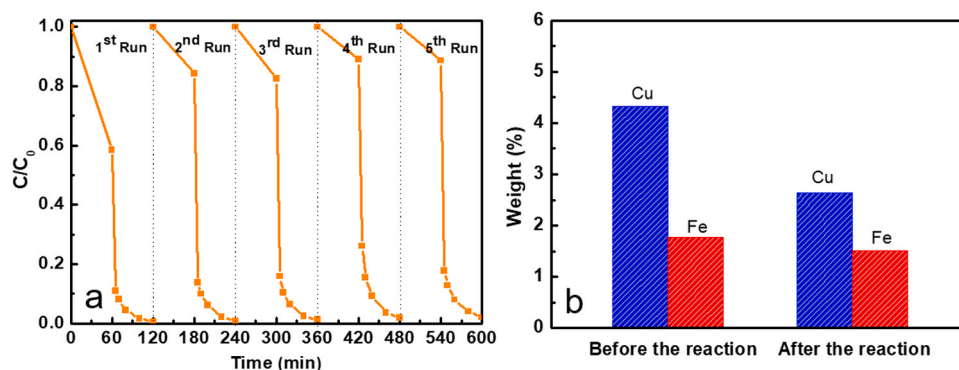


Fig. 7. (a) Stability tests of CuFeO QDs/CNNSSs for TC degradation, (b) weight comparison of Cu and Fe before and after five cycles. [Conditions: initial pH = 6.0; H₂O₂ = 100.0 mM; TC = 50 mg L⁻¹, catalyst dosage = 0.5 g L⁻¹].

The effect of initial TC concentrations (10–70 mg/L) was illustrated in Fig. 6e. We found that the degradation rates of TC decreased gradually with the increase of TC concentrations. When its initial concentration was 70 mg/L, a degradation efficiency of 99.7% was still reached, implying the lasting high degradation efficiency of CuFeO QDs/CNNSSs.

In addition, Fig. 6f testified the universal applicability of CuFeO QDs/CNNSSs towards various pollutants. Rhodamine B (RhB), p-nitro-phenol (PNP) and Cr (VI) could be effectively removed with up to ≈100.0%, 98.2% and 97.4%, respectively, confirming the excellent catalytic performance of CuFeO QDs/CNNSSs for different pollutants. The difference

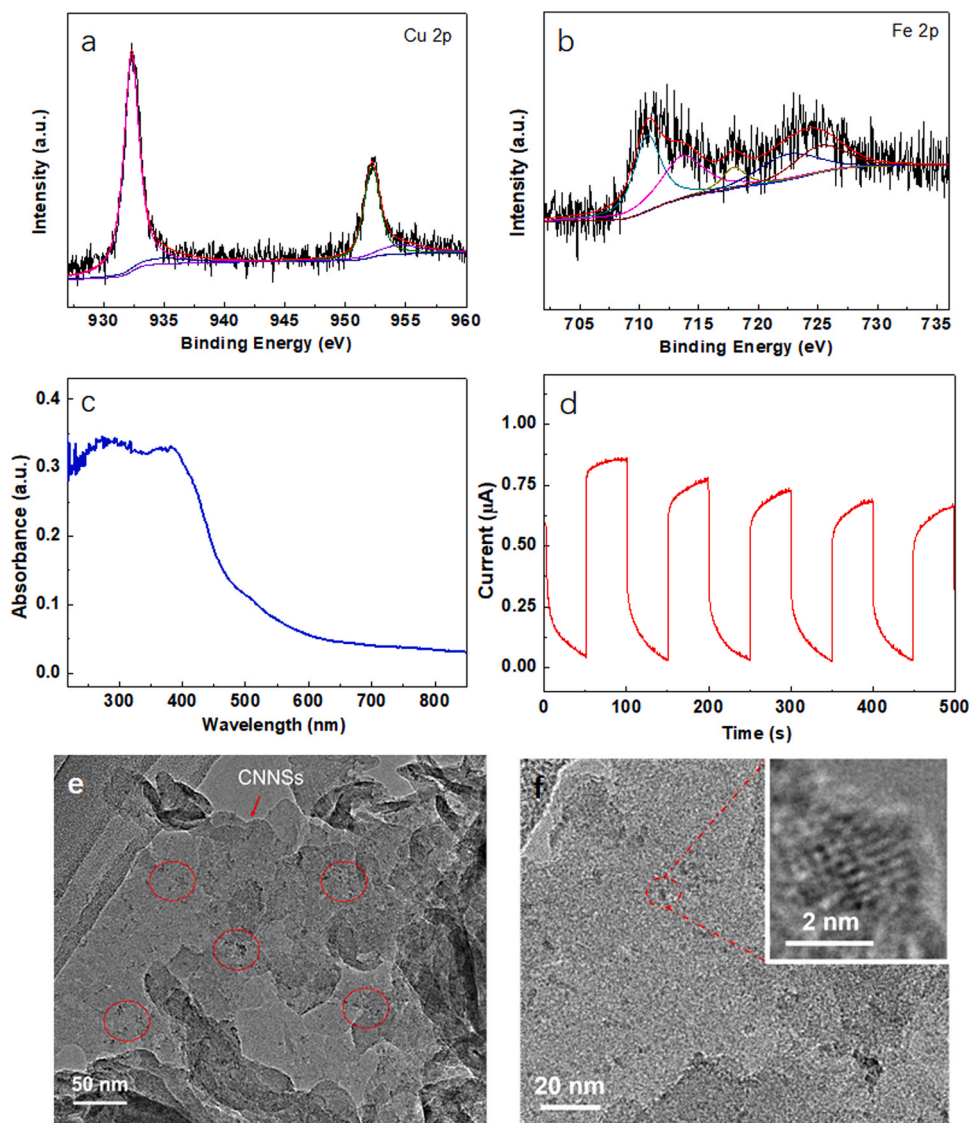


Fig. 8. (a, b) XPS spectra of Cu 2p and Fe 2p, (c) UV-vis DRS, (d) transient photocurrent performance, (e and f) TEM images of used CuFeO QDs/CNNs hybrid after the 1st run.

in degradation efficiency of different pollutants may be due to multiple factors, such as different degradation mechanisms, difficulty of degradation derived from the different bond energies of pollutants, and different adsorption capacities of CuFeO QDs/CNNs toward these pollutants. In addition, the activity of our CuFeO QDs/CNNs catalyst is much superior to that of many reports on Fe/Cu-based photo-Fenton catalysts (Table S2), manifesting the advantage of our 0D/2D catalyst with bi-metal sites over the traditional Fe/Cu nanoparticles supported on CNNs in photo-Fenton reaction.

The stability of the catalyst is of great importance to its practical applications. Therefore, the catalytic stability of CuFeO QDs/CNNs was evaluated by recycling TC degradation. As shown in Fig. 7a, a slight decrease in degradation rate of CuFeO QDs/CNNs was observed after five cycles, but the TC total removal efficiency still maintained 98%. After the 1st run, the morphology and microstructure, surface chemical states, optical and photoelectric properties of used CuFeO QDs/CNNs almost unchanged compared to pristine catalysts (Fig. 8 and Fig. S10). However, the adsorption performance of CuFeO QDs/CNNs declined after the 1st run, which might be due to partial occupation of adsorption sites by TC and fractional loss of Cu and Fe species. Fig. 7b depicted the total Cu and Fe amounts of CuFeO QDs/CNNs before (4.33 wt% for Cu, 1.78 wt% for Fe) and after five cycles (2.64 wt% for Cu, 1.55 wt% for

Fe). The loss of Cu content had little effect on TC total removal efficiency, which may be due to the synergy of photocatalysis and Fenton oxidation. In the case of partial loss of Cu and Fe contents, the contribution of photocatalytic degradation may increase, which still could ensure producing enough active free radicals to degrade TC. As illustrated in Fig. S11, the photoelectric properties of CuFeO QDs/CNNs after five cycles was similar to pristine sample. Homogeneously dispersed QDs still could be clearly observed on the surface of CNNs (Fig. S11), indicating that the catalyst still maintained favorable 0D/2D structure. The above results revealed an outstanding reusability of CuFeO QDs/CNNs, indicating the great potential of CuFeO QDs/CNNs for wastewater treatment in practical application.

The catalytic mechanism was investigated by testing the active species involved in CuFeO QDs/CNNs-H₂O₂/visible light system. Various radical scavengers, such as TBA, FFA, AgNO₃, AO and BQ, were selected to trap •OH, ¹O₂, e⁻, h⁺ and O₂^{•+}, respectively [2]. Fig. 9a witnessed that the addition of AgNO₃ had almost no effect on the degradation of TC, which indicated that e⁻ was not responsible for TC degradation. In the presence of redundant TBA or AO, the degradation efficiency slightly decreased, further indicating that •OH and h⁺ were involved in this reaction, but not the primary reactive species. Considering weak direct photolysis of H₂O₂ and more negative position of E_{VB}

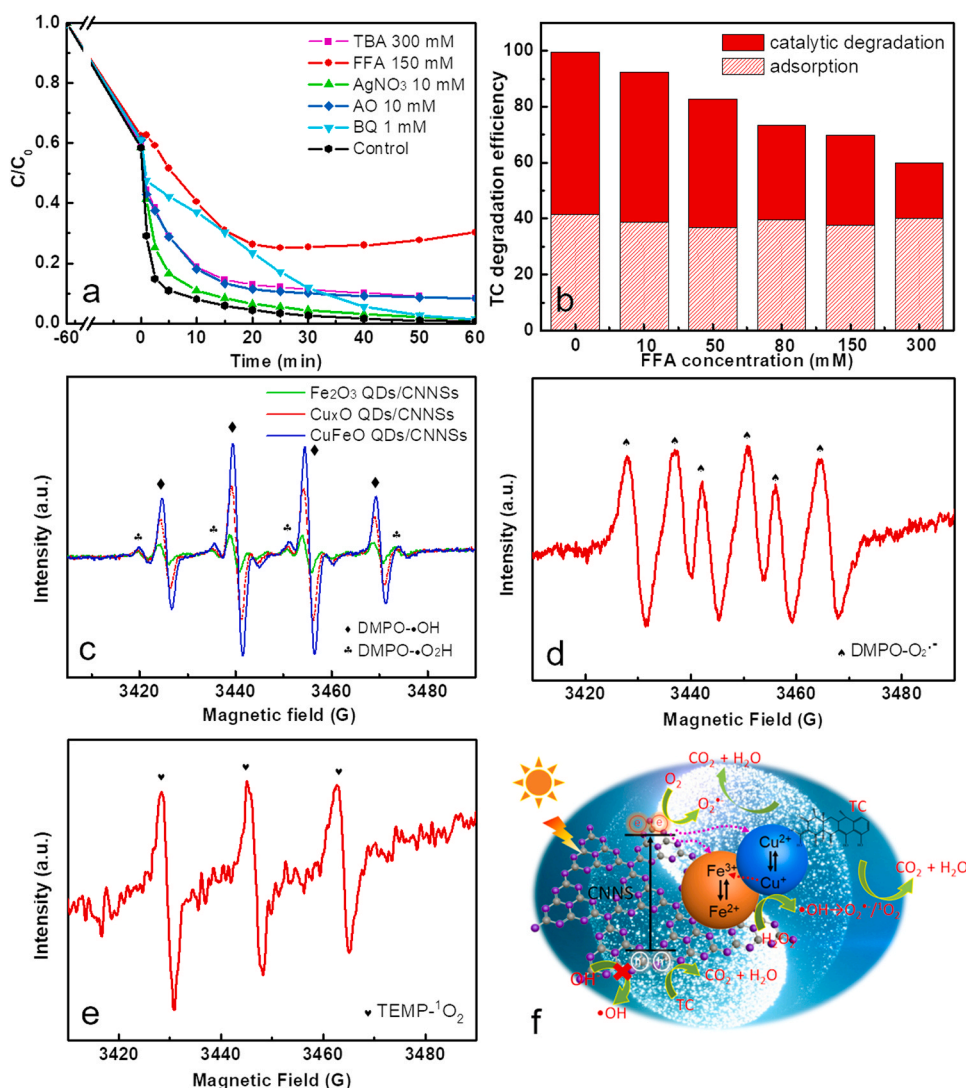
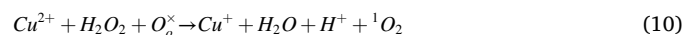
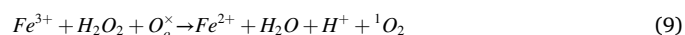
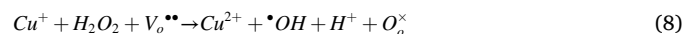
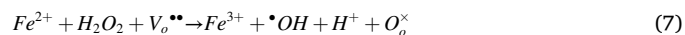


Fig. 9. (a) Control experiments using different radical scavengers, (b) ¹O₂ trapping experiments with different FFA concentrations, ESR spectra of (c) DMPO/•OH in H₂O solution, (d) DMPO/O₂•⁻ in methanol solution, (e) TEMP/¹O₂ in H₂O solution for H₂O₂ activation over different hybrids, and (f) schematic illustration of catalytic mechanism of CuFeO QDs/CNNs in H₂O₂/visible light system. [Conditions: catalyst dosage = 0.5 g L⁻¹; H₂O₂ = 100.0 mM; DMPO = 100.0 mM; TEMP = 100.0 mM, T = 25 °C and initial pH = 6.0].

of CNNs (+1.51 eV) than OH[•]/•OH potential (+1.99 eV) [46], a certain amount of •OH might be generated by Fe²⁺/Cu⁺-catalyzed H₂O₂ activation process. However, when BQ or FFA was added into the system, an obvious inhibition effect for TC degradation was observed, indicated that O₂•⁻ and ¹O₂ played main roles in TC degradation. Moreover, the TC degradation efficiency reduced remarkably from 92.2% to 59.9% as the concentrations of FFA increased from 10 mM to 300 mM (Fig. 9b), further indicating that ¹O₂ acted as a dominant active species in this system. In in situ EPR spin trapping tests, 5,5-dimethyl-1-pyrroline-N-oxide (DMPO) and 2,2,6,6-tetramethyl-4-piperidinol (TEMP) were selected as spin trap agents [47]. In Fig. 9c-e, the signal peaks of DMPO-•OH (four characteristic peaks with the intensity ratios of 1:2:2:1), DMPO-O₂•⁻ and TEMP-¹O₂ (three-line typical EPR spectra) were discerned as the generation of •OH, O₂•⁻ and ¹O₂ in CuFeO QDs/CNNs-H₂O₂ system under light irradiation. For comparison, Fe₂O₃ QDs/CNNs-H₂O₂ and Cu_xO QDs/CNNs-H₂O₂ systems were also detected by EPR. Obviously, the intensity of •OH (Fig. 9c) in CuFeO QDs/CNNs-H₂O₂ system were much greater than that in Fe₂O₃ QDs/CNNs-H₂O₂ and Cu_xO QDs/CNNs-H₂O₂ systems, demonstrating higher H₂O₂ activation performance of CuFeO QDs/CNNs than single metal oxides QDs-CNNs hybrids. The signals of DMPO-O₂•⁻ and TEMP-¹O₂ in Fig. 9d-e confirmed the existence of abundant O₂•⁻ and ¹O₂. Due to more negative position of E_{CB} of CNNs (-1.24 eV) than O₂/O₂•⁻ potential (-0.33 eV) and better charge separation in CuFeO QDs/CNNs

hybrid, it was expected that O₂•⁻ played an important role in TC degradation. In addition, Fe₂O₃ QDs/CNNs and Cu_xO QDs/CNNs samples also showed the formation of ¹O₂ in catalytic process (Fig. S12), revealing that ¹O₂ was mainly derived from the reactions of other intermediate radicals. Furthermore, it was reported that surface oxygen vacancies (V_o••) could promote the formation of ¹O₂ [47]. Therefore, the catalytic mechanism of CuFeO QDs/CNNs-H₂O₂ system under light irradiation was illustrated in Fig. 9f, which could be expressed by reactions as follows:



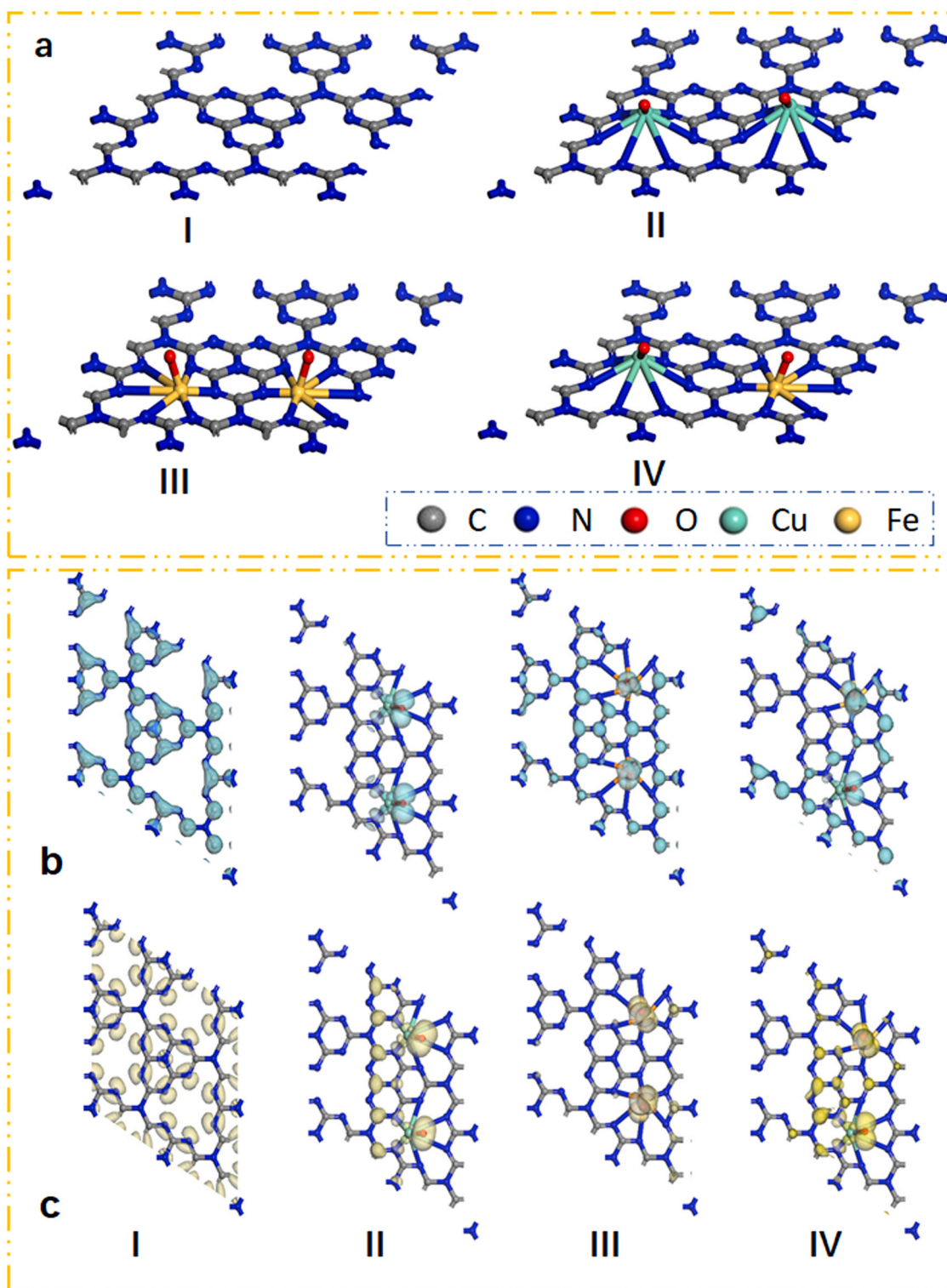
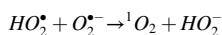
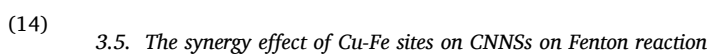
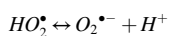
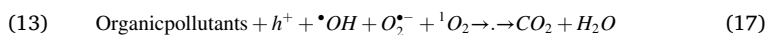
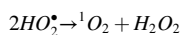


Fig. 10. (a) DFT-optimized structure, (b) LUMO and (c) HOMO orbitals of (I) CNNSs, (II) Cu_xO QDs/CNNSs, (III) Fe₂O₃ QDs/CNNSs and (IV) CuFeO QDs/CNNSs (CNNSs substrate was an infinitely extended structure).



(15) Considering the incremental catalytic activity of CuFeO QDs/CNNSs hybrid for photo-Fenton reaction, except for the above confirmed fast photogenerated charge separation and transfer, the synergistic effect of

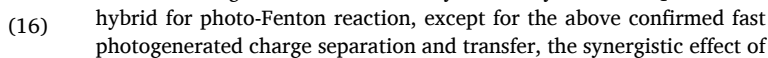
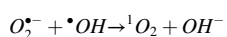


Table 3

The absorption parameters of H_2O_2 and $\bullet\text{OH}$ on CNNSs, Fe_2O_3 QDs/CNNs, Cu_xO QDs/CNNs and CuFeO QDs/CNNs.

	H_2O_2	CNNs	Fe_2O_3 QDs/ CNNs	Cu_xO QDs/ CNNs	CuFeO QDs/CNNs
HOMO-LUMO gap (eV)	–	1.17	0.08	0.18	0.11
H_2O_2 absorption energy (eV)	–	-0.23	-1.12	-2.93	-1.40
O-O bond length (Å)	1.47	–	1.52	1.30	1.48
$\bullet\text{OH}$ absorption energy (eV)	–	-0.33	-2.30	-1.51	-1.56

Cu and Fe sites on Fenton reaction was revealed in depth by DFT calculations (Fig. 10). The highest occupied molecular orbital (HOMO), the lowest unoccupied molecular orbital (LUMO) and the HOMO-LUMO gaps of the samples were calculated. As listed in Table 3, the HOMO-LUMO gap of CNNs was 1.17 eV. After introducing the metallic oxide QDs, the HOMO-LUMO gaps were decreased to 0.18 eV for Cu_xO QDs/CNNs and 0.08 eV for Fe_2O_3 QDs/CNNs, which indicated that the electron transfer was accelerated between QDs and CNNs. The density of state (DOS) near the Fermi level (E_f) also showed that the intensity of electron level distribution of hybrid catalysts was greatly improved compared with pristine CNNs, indicating the faster migration rate of electrons (Fig. 11a-b) [48]. Fig. 10b and c displayed that the electron density mainly localized on Cu and Fe sites, which would dynamically enhance the electron exchange between H_2O_2 and Cu_xO or Fe_2O_3 QDs, resulting in the promoted decomposition of H_2O_2 [49]. Fe sites on CNNs possessed more outstanding ability towards H_2O_2 activation than Cu sites. The HOMO-LUMO gap of CuFeO QDs/CNNs (0.11 eV) was far

less than that of Cu_xO QDs/CNNs (0.18 eV), suggesting that the incorporation of a small number of Fe sites could significantly promote H_2O_2 decomposition. The change in bond length of O-O bond in H_2O_2 after the adsorption on different catalysts further confirmed the easy H_2O_2 activation by combining Fe_2O_3 and Cu_xO QDs on CNNs. Furthermore, H_2O_2 absorption on Cu and Fe sites was also investigated based on DFT calculations. As shown in Fig. 11c, the bond length for H_2O_2 adsorbed on the surface of catalysts was defined as the distance between H atom in H_2O_2 and O atom bound to metal atom, which was represented by the dotted lines. Herein, 0.98 Å and 0.98 Å were the distances of O atom bound to two different Cu atoms in the triazine ring of CNNs (002) plane in Cu_xO QDs/CNNs to H atom whereas 1.76 Å and 1.99 Å were the distances of the two H-O on Fe_2O_3 QDs/CNNs, respectively. The shorter distances for single Cu_xO QDs/CNNs indicated a stronger H_2O_2 adsorption ability than Fe_2O_3 QDs/CNNs. For CuFeO QDs/CNNs, the distances of H-O-Cu and H-O-Fe were 1.01 Å and 2.73 Å, respectively, manifesting Cu species were the main H_2O_2 adsorption sites. Moreover, the absorption energies of H_2O_2 on catalysts were as follows: Cu_xO QDs/CNNs (-2.93 eV) > CuFeO QDs/CNNs (-1.40 eV) > Fe_2O_3 QDs/CNNs (-1.12 eV), demonstrating that the incorporation of Cu species into the Fe oxide could enhance H_2O_2 adsorption ability. As shown in Fig. 11a-b, the d-band centers of hybrids were more far away from E_f than that (-7.29 eV) in CNNs, suggesting a downshift in d-band center when Cu_xO QDs or Fe_2O_3 QDs were anchored on CNNs [50]. As the d-band center is intervenient between anti-bonding and bonding, it would be a good descriptor of the strength of H-O-metal binding [51]. When the d-band center downshifts, the energy level of antibonding states is lowered and the interaction between adsorbate and surface is weakened, which is not favor to H_2O_2 adsorption. The d-band center (E_d) of Fe_2O_3 QDs/CNNs, Cu_xO QDs/CNNs and CuFeO QDs/CNNs were calculated to be -8.29 eV, -7.61 eV and -8.08 eV, respectively, indicating that the addition of Cu species could

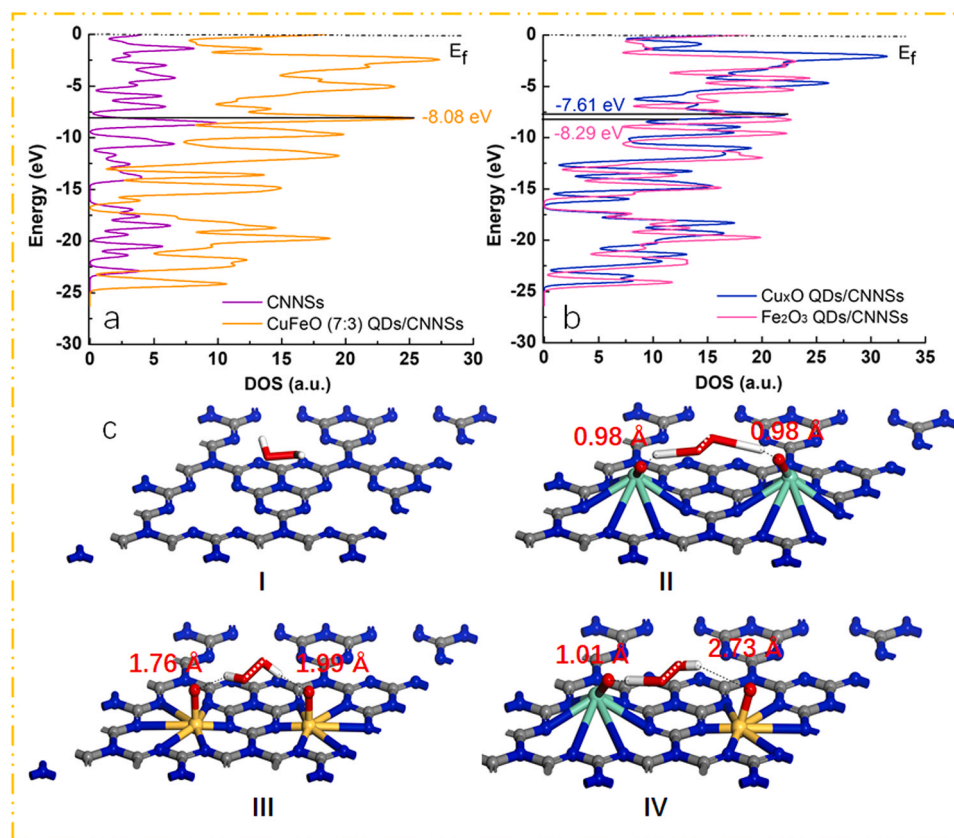


Fig. 11. (a, b) Density of states for Fe_2O_3 QDs/CNNs, Cu_xO QDs/CNNs and CuFeO QDs/CNNs (d-band centers are highlighted in the DOS curves), (c) H_2O_2 absorption on (I) CNNs, (II) Cu_xO QDs/CNNs, (III) Fe_2O_3 QDs/CNNs and (IV) CuFeO QDs/CNNs's Cu-Fe sites.

facilitate H_2O_2 adsorption on the surface of catalyst. This was agreement with the results of absorption energy. Adsorption and activation of H_2O_2 are two critical factors for enhancing Fenton reactivity. CuFeO QDs/CNNs combined the unique advantages of both Cu and Fe species, (i.e. splendid H_2O_2 adsorption for Cu sites and outstanding H_2O_2 activation for Fe species). The synergy of Cu and Fe sites could achieve the optimal coordination between H_2O_2 adsorption and activation in Fenton reaction, which thus could overcome the discordance of H_2O_2 adsorption and activation in single-Cu or Fe oxide/CNNs hybrid. It is well known that the rapid release of generated free radicals from catalyst surface can accelerate the degradation of pollutants. Although H_2O_2 could be activated easily on Fe sites of Fe_2O_3 QDs/CNNs, it showed poor desorption ability towards $\bullet\text{OH}$ derived from the direct decomposition of H_2O_2 catalyzed by Fenton reaction (Fig. S13, Table 3), which hindered the subsequent formation of $^1\text{O}_2$ radicals and therefore reduced the degradation efficiency towards pollutants. Excitingly, the coexistence of Cu and Fe sites on CNNs could take advantage of superior $\bullet\text{OH}$ desorption of Cu species, and accelerate the release of $\bullet\text{OH}$, leading to more reactive oxygen species to take part in degradation reaction. Based on the above discussion, multiple synergies of H_2O_2 adsorption and activation and the release of generated free radicals contributed to the incremental Fenton activity.

Therefore, this newly developed Cu-Fe bi-metal oxide QDs/CNNs hybrid exhibited multiple unique advantages beyond single-metal OD/2D counterparts. The coexistence of Cu-Fe sites not merely promoted photoelectric properties, but also modified TC absorption and achieved H_2O_2 adsorption-activation trade-off on catalyst surface, which led to dual coordination between adsorption-catalytic degradation and photocatalysis-Fenton oxidation. In addition, it's worth noting that this facile one-step synthesis technology can be extended to obtain other multi-metal oxides QDs on CNNs, such as Co, Ni and Sn-based oxides QDs, which will have great potential in many frontier fields, not limited to photo-Fenton catalysis.

4. Conclusion

In this work, a novel OD/2D CuFeO QDs/CNNs hybrid with multi-metal sites was fabricated via a facile one-step synthesis strategy for photo-Fenton catalysis. Plenty of ultrafine CuFeO QDs were tightly decorated onto hierarchical CNNs surfaces to form heterojunction structure, which not only provided more available Cu/Fe sites but also expedited dramatically the charge separation and transfer. Except for the above advantages, the synergy of Cu and Fe sites on CNNs could also modify TC absorption capacity of CuFeO QDs/CNNs, and optimize the coordination between H_2O_2 adsorption and activation on Cu-Fe sites making H_2O_2 activation more easy, which simultaneously promoted multiple synergies of adsorption-catalytic degradation and photocatalysis-Fenton oxidation and then achieved a significant improvement in pollutant removal efficiency. In addition, CuFeO QDs/CNNs also showed a good long-term stability. Therefore, this work will provide new insights in developing multi-functional OD/2D hybrids for extensive environment and energy applications.

CRedit authorship contribution statement

M.E. Liu: Investigation, methodology, Writing – original draft. **H. Xia:** Supervision, Methodology, Writing – review original draft. **W.X. Yang, X.Y. Liu and J. Xiang:** Formal analysis. **X.M. Wang and L.S. Hu:** Analysis tools. **F.S. Lu:** Supervision, methodology and Writing – review original draft.

Declaration of Competing Interest

The authors declare that they have no known competing financial interests or personal relationships that could have appeared to influence the work reported in this paper.

Acknowledgments

This work is supported by Natural Science Foundation of China (21671127), Guangdong Natural Science Foundation (2019A1515012156 and 2019A1515010076), Major Project of Guangdong Department of Education (2017KZDXM034), Scientific Research Foundation of Shantou University (NTF20005), The Characteristic Innovation Project of Colleges and Universities in Guangdong (2021KTSCX030, 2021LSYS009 and 2021KCXTD032), 2020 Li Ka Shing Foundation Cross-Disciplinary Research Grant (2020LKSFG01A).

Appendix A. Supporting information

Supplementary data associated with this article can be found in the online version at doi:10.1016/j.apcatb.2021.120765.

References

- [1] X. Wang, X. Zhang, Y. Zhang, Y. Wang, S.P. Sun, W.D. Wu, Z. Wu, Nanostructured semiconductor supported iron catalysts for heterogeneous photo-Fenton oxidation: a review, *J. Mater. Chem. A* 8 (2020) 15513–15546, <https://doi.org/10.1039/D0TA04541A>.
- [2] H. Xia, Z. Zhang, J. Liu, X. Ning, S. Zhang, X. Lu, Developing superior catalysts engineered by multichannel healing strategy for advanced oxidation, *Appl. Catal. B: Environ.* 250 (2019) 189–199, <https://doi.org/10.1016/j.apcatb.2019.03.033>.
- [3] G. Liu, T. Zhang, T. Wang, H. Yamashita, Y. Zhao, X. Qian, Peroxydisulfate activation by photo-generated charges on mesoporous carbon nitride for removal of chlorophenols, *Appl. Catal. B: Environ.* 296 (2021), 120370, <https://doi.org/10.1016/j.apcatb.2021.120370>.
- [4] L. Zhu, J. Ji, J. Liu, S. Mine, M. Matsuoka, J. Zhang, M. Xing, Designing 3D-MoS₂ sponge as excellent cocatalysts in advanced oxidation processes for pollutant control, *Angew. Chem. Int. Ed.* 59 (2020) 13968–13976, <https://doi.org/10.1002/anie.202006059>.
- [5] W. Zhao, I.W. Chen, F. Huang, Toward large-scale water treatment using nanomaterials, *Nano Today* 27 (2019) 11–27, <https://doi.org/10.1016/j.nantod.2019.05.003>.
- [6] F. Li, T. Li, L. Zhang, Y. Jin, C. Hu, Enhancing photocatalytic performance by direct photo-excited electron transfer from organic pollutants to low-polymerized graphitic carbon nitride with more C-NH/NH₂ exposure, *Appl. Catal. B: Environ.* 296 (2021), 120316, <https://doi.org/10.1016/j.apcatb.2021.120316>.
- [7] S. Yang, S. Xu, J. Tong, D. Ding, G. Wang, R. Chen, P. Jin, X. Wang, Overlooked role of nitrogen dopant in carbon catalysts for peroxymonosulfate activation: intrinsic defects or extrinsic defects? *Appl. Catal. B: Environ.* 295 (2021), 120291, <https://doi.org/10.1016/j.apcatb.2021.120291>.
- [8] K. Qi, Xi Xing, A. Zada, M. Li, Q. Wang, S. Liu, H. Lin, G. Wang, Transition metal doped ZnO nanoparticles with enhanced photocatalytic and antibacterial performances: experimental and DFT studies, *Ceram. Int.* 46 (2020) 1494–1502, <https://doi.org/10.1016/j.ceramint.2019.09.116>.
- [9] T. Li, Y. Chen, X. Wang, J. Liang, L. Zhou, Modifying organic carbon in Fe₃O₄-loaded schwertmannite to improve heterogeneous Fenton activity through accelerating Fe(II) generation, *Appl. Catal. B: Environ.* 285 (2021), 119830, <https://doi.org/10.1016/j.apcatb.2020.119830>.
- [10] J. Liang, X. Duan, X. Xu, K. Chen, F. Wu, H. Qiu, C. Liu, S. Wang, X. Cao, Biomass-derived pyrolytic carbons accelerated Fe(III)/Fe(II) redox cycle for persulfate activation: pyrolysis temperature-dependent performance and mechanisms, *Appl. Catal. B: Environ.* 297 (2021), 120446, <https://doi.org/10.1016/j.apcatb.2021.120446>.
- [11] S. Karthikeyan, M.P. Pachamuthu, M.A. Isaacs, S. Kumar, A.F. Lee, G. Sekaran, Cu and Fe oxides dispersed on SBA-15: a Fenton type bimetallic catalyst for N,N-diethyl-p-phenyl diamine degradation, *Appl. Catal. B: Environ.* 199 (2016) 323–330, <https://doi.org/10.1016/j.apcatb.2016.06.040>.
- [12] H. Xia, Z. Zhang, J. Liu, Y. Deng, D. Zhang, P. Du, S. Zhang, X. Lu, Novel Fe-Mn-O nanosheets/wood carbon hybrid with tunable surface properties as a superior catalyst for Fenton-like oxidation, *Appl. Catal. B: Environ.* 259 (2019), 118058, <https://doi.org/10.1016/j.apcatb.2019.118058>.
- [13] Z. Wan, J. Wang, Degradation of sulfamethazine using Fe₃O₄-Mn₃O₄/reduced graphene oxide hybrid as Fenton-like catalyst, *J. Hazard. Mater.* 324 (2017) 653–664, <https://doi.org/10.1016/j.jhazmat.2016.11.039>.
- [14] G.W. Woyessa, J.B. dela Cruz, M. Rameez, C.H. Hung, Nanocomposite catalyst of graphitic carbon nitride and Cu/Fe mixed metal oxide for electrochemical CO₂ reduction to CO, *Appl. Catal. B: Environ.* 291 (2021), 120052, <https://doi.org/10.1016/j.apcatb.2021.120052>.
- [15] J. Liu, P. Wu, S. Yang, S. Rehman, Z. Ahmed, N. Zhu, Z. Dang, Z. Liu, A photo-switch for peroxydisulfate non-radical/radical activation over layered CuFe oxide: Rational degradation pathway choice for pollutants, *Appl. Catal. B: Environ.* 261 (2020), 118232, <https://doi.org/10.1016/j.apcatb.2019.118232>.
- [16] M.Y. Ye, Z.H. Zhao, Z.F. Hu, L.Q. Liu, H.M. Ji, Z.R. Shen, T.Y. Ma, OD/2D heterojunctions of vanadate quantum dots/Graphitic carbon nitride nanosheets for enhanced visible-light-driven photocatalysis, *Angew. Chem. Int. Ed.* 56 (2017) 8407–8411, <https://doi.org/10.1002/anie.201611127>.

- [17] H. Gao, H. Yang, J. Xu, S. Zhang, J. Li, Strongly coupled g-C₃N₄ nanosheets-Co₃O₄ quantum dots as 2D/0D heterostructure composite for peroxymonosulfate activation, *Small* 14 (2018), 1801353, <https://doi.org/10.1002/sml.201801353>.
- [18] H. Xia, C. Hong, B. Li, B. Zhao, Z. Lin, M. Zheng, S.V. Savilov, S.M. Aldoshin, Facile synthesis of hematite quantum-dot/functionalized graphene-sheet composites as advanced anode materials for asymmetric supercapacitors, *Adv. Funct. Mater.* 25 (2015) 627–635, <https://doi.org/10.1002/adfm.201403554>.
- [19] J. Liu, M. Zheng, X. Shi, H. Zeng, H. Xia, Amorphous FeOOH quantum dots assembled mesoporous film anchored on graphene nanosheets with superior electrochemical performance for supercapacitors, *Adv. Funct. Mater.* 26 (2016) 919–930, <https://doi.org/10.1002/adfm.201504019>.
- [20] Z. Fang, Y. Wang, J. Song, Y. Sun, J. Zhou, R. Xu, H. Duan, Immobilizing CdS quantum dots and dendritic Pt nanocrystals on thiolated graphene nanosheets toward highly efficient photocatalytic H₂ evolution, *Nanoscale* 5 (2013) 9830–9838, <https://doi.org/10.1039/C3NR03043A>.
- [21] F.X. Xiao, J. Miao, B. Liu, Layer-by-layer self-assembly of CdS quantum dots/graphene nanosheets hybrid films for photoelectrochemical and photocatalytic applications, *J. Am. Chem. Soc.* 136 (2014) 1559–1569, <https://doi.org/10.1021/ja411651e>.
- [22] J. Xu, Q. Gao, Z. Wang, Y. Zhu, An all-organic 0D/2D supramolecular porphyrin/g-C₃N₄ heterojunction assembled via π - π interaction for efficient visible photocatalytic oxidation, *Appl. Catal. B: Environ.* 291 (2021), 120059, <https://doi.org/10.1016/j.apcatb.2021.120059>.
- [23] W. Li, C. Zhuang, Y. Li, C. Gao, W. Jiang, Z. Sun, K. Qi, Anchoring ultra-small TiO₂ quantum dots onto ultra-thin and large-sized Mxene nanosheets for highly efficient photocatalytic water splitting, *Ceram. Int.* 47 (2021) 21769–21776, <https://doi.org/10.1016/j.ceramint.2021.04.192>.
- [24] K. Qi, S. Liu, A. Zada, Graphitic carbon nitride, a polymer photocatalyst, *J. Taiwan Inst. Chem. Eng.* 109 (2020) 111–123, <https://doi.org/10.1016/j.jtice.2020.02.012>.
- [25] J. Xi, H. Xia, X. Ning, Z. Zhang, X. Lu, Carbon-intercalated 0D/2D hybrid of hematite quantum dots/graphitic carbon nitride nanosheets as superior catalyst for advanced oxidation, *Small* 15 (2019), 1902744, <https://doi.org/10.1002/sml.201902744>.
- [26] G. Shen, L. Pan, R. Zhang, S. Sun, F. Hou, X. Zhang, J.J. Zou, Low-spin-state hematite with superior adsorption of anionic contaminations for water purification, *Adv. Mater.* 32 (2020), 1905988, <https://doi.org/10.1002/adma.201905988>.
- [27] Q. Guo, Y. Zhang, H.S. Zhang, Y. Liu, Y.J. Zhao, J. Qiu, G. Dong, 3D foam strutted graphene carbon nitride with highly stable optoelectronic properties, *Adv. Funct. Mater.* 27 (2017), 1703711, <https://doi.org/10.1002/adfm.201703711>.
- [28] K. Qi, N. Cui, M. Zhang, Y. Ma, G. Wang, Z. Zhao, A. Khataee, Ionic liquid-assisted synthesis of porous boron-doped graphitic carbon nitride for photocatalytic hydrogen production, *Chemosphere* 272 (2021), 129953, <https://doi.org/10.1016/j.chemosphere.2021.129953>.
- [29] K. Qi, A. Zada, Y. Yang, Q. Chen, A. Khataee, Design of 2D–2D NiO/g-C₃N₄ heterojunction photocatalysts for degradation of an emerging pollutant, *Res. Chem. Intermed.* 46 (2020) 5281–5295, <https://doi.org/10.1007/s11164-020-04262-0>.
- [30] K. Qi, W. Lv, I. Khan, S. Liu, Photocatalytic H₂ generation via CoP quantum-dot-modified g-C₃N₄ synthesized by electroless plating, *Chin. J. Catal.* 41 (2020) 114–121, (<http://www.sciencedirect.com/science/journal/18722067>).
- [31] Z. Huang, X. Zhao, H. Xia, F. Lu, L. Hu, P.K. Chu, Insights into enhancement of photocatalytic properties of g-C₃N₄ by local electric field induced by polarization of MgO (111), *J. Environ. Chem. Eng.* 9 (2021), 105922, <https://doi.org/10.1016/j.jece.2021.105922>.
- [32] K. Cao, H. Liu, W. Li, Q. Han, Z. Zhang, K. Huang, Q. Jing, L. Jiao, CuO nanoplates for high-performance potassium-ion batteries, *Small* 15 (2019), 1901775, <https://doi.org/10.1002/sml.201901775>.
- [33] L. Zhao, Y. Qi, L. Song, S. Ning, S. Ouyang, H. Xu, J. Ye, Solar-driven water-gas shift reaction over CuO_x/Al₂O₃ with 1.1% of light-to-energy storage, *Angew. Chem. Int. Ed.* 58 (2019) 7708–7712, <https://doi.org/10.1002/anie.201902324>.
- [34] L. Wang, X. Zhang, X. Yu, F. Gao, Z. Shen, X. Zhang, S. Ge, J. Liu, Z. Gu, C. Chen, An all-organic semiconductor C₃N₄/PDINH heterostructure with advanced antibacterial photocatalytic therapy activity, *Adv. Mater.* 31 (2019), 1901965, <https://doi.org/10.1002/adma.201901965>.
- [35] N. Tian, H. Huang, C. Liu, F. Dong, T. Zhang, X. Du, S. Yu, Y. Zhang, In situ copolyrolysis fabrication of CeO₂/g-C₃N₄ n-n type heterojunction for synchronously promoting photo-induced oxidation and reduction properties, *J. Mater. Chem. A* 3 (2015) 17120–17129, <https://doi.org/10.1039/C5TA03669K>.
- [36] G. Zhang, Z. Wu, H. Liu, Q. Ji, J. Qu, J. Li, Photoactivation healing of α -FeOOH@g-C₃N₄ catalyst for efficient and stable activation of persulfate, *Small* 13 (2017), 1702225, <https://doi.org/10.1002/sml.201702225>.
- [37] J. Xu, Q. Ji, X. Yan, C. Wang, L. Wang, Ni(acac)₂/Mo-MOF-derived difunctional MoNi@MoO₃ cocatalyst to enhance the photocatalytic H₂ evolution activity of g-C₃N₄, *Appl. Catal. B: Environ.* 268 (2020), 118739, <https://doi.org/10.1016/j.apcatb.2020.118739>.
- [38] Z. Zhang, H. Wu, Z. Yu, R. Song, K. Qian, X. Chen, J. Tian, W. Zhang, W. Huang, Site-resolved Cu₂O catalysis in the oxidation of CO, *Angew. Chem. Int. Ed.* 58 (2019) 4276–4280, <https://doi.org/10.1002/anie.201814258>.
- [39] I. Platzman, R. Brenner, H. Haick, R. Tannenbaum, Oxidation of polycrystalline copper thin films at ambient conditions, *J. Phys. Chem. C* 112 (2008) 1101–1108, <https://doi.org/10.1021/jp076981k>.
- [40] R. Li, M. Cai, Z. Xie, Q. Zhang, Y. Zeng, H. Liu, G. Liu, W. Lv, Construction of heterostructured CuFe₂O₄/g-C₃N₄ nanocomposite as an efficient visible light photocatalyst with peroxydisulfate for the organic oxidation, *Appl. Catal. B: Environ.* 244 (2019) 974–982, <https://doi.org/10.1016/j.apcatb.2018.12.043>.
- [41] J. Wang, Y. Xia, H. Zhao, G. Wang, L. Xiang, J. Xu, S. Komarneni, Oxygen defects-mediated Z-scheme charge separation in g-C₃N₄/ZnO photocatalysts for enhanced visible-light degradation of 4-chlorophenol and hydrogen evolution, *Appl. Catal. B: Environ.* 206 (2017) 406–416, <https://doi.org/10.1016/j.apcatb.2017.01.067>.
- [42] F. Chen, Q. Yang, Y. Wang, J. Zhao, D. Wang, X. Li, Z. Guo, H. Wang, Y. Deng, C. Niu, G. Zeng, Novel ternary heterojunction photocatalyst of Ag nanoparticles and g-C₃N₄ nanosheets co-modified BiVO₄ for wider spectrum visible-light photocatalytic degradation of refractory pollutant, *Appl. Catal. B: Environ.* 205 (2017) 133–147, <https://doi.org/10.1016/j.apcatb.2016.12.017>.
- [43] J. Jiang, X. Wang, Y. Liu, Y. Ma, T. Li, Y. Lin, T. Xie, S. Dong, Photo-Fenton degradation of emerging pollutants over Fe-POM nanoparticle/porous and ultrathin g-C₃N₄ nanosheet with rich nitrogen defect: degradation mechanism, pathways, and products toxicity assessment, *Appl. Catal. B: Environ.* 278 (2020), 119349, <https://doi.org/10.1016/j.apcatb.2020.119349>.
- [44] F. Chen, W. An, L. Liu, Y. Liang, W. Cui, Highly efficient removal of bisphenol A by a three-dimensional graphene hydrogel-AgBr@GO exhibiting adsorption/photocatalysis synergy, *Appl. Catal. B: Environ.* 217 (2017) 65–80, <https://doi.org/10.1016/j.apcatb.2017.05.078>.
- [45] H. Xia, D. Qin, X. Zhou, X. Liu, X. Lu, Ion transport traversing bioinspired ion channels at bionic interface, *J. Phys. Chem. C* 117 (2013) 23522–23528, <https://doi.org/10.1021/jp407760m>.
- [46] F. Chen, Q. Yang, S. Wang, F. Yao, J. Sun, Y. Wang, C. Zhang, X. Li, C. Niu, D. Wang, G. Zeng, Graphene oxide and carbon nitride nanosheets co-modified silver chromate nanoparticles with enhanced visible-light photoactivity and anti-photocorrosion properties towards multiple refractory pollutants degradation, *Appl. Catal. B: Environ.* 209 (2017) 493–505, <https://doi.org/10.1016/j.apcatb.2017.03.026>.
- [47] J. Li, J. Miao, X. Duan, J. Dai, Q. Liu, S. Wang, W. Zhou, Z. Shao, Fine-tuning surface properties of perovskites via nanocompositing with inert oxide toward developing superior catalysts for advanced oxidation, *Adv. Funct. Mater.* 28 (2018), 1804654, <https://doi.org/10.1002/adfm.201804654>.
- [48] Y. Li, X. Xu, J. Wang, W. Luo, Z. Zhang, X. Cheng, J. Wu, Y. Yang, G. Chen, S. Sun, L. Wang, Post-redox engineering electron configurations of atomic thick C₃N₄ nanosheets for enhanced photocatalytic hydrogen evolution, *Appl. Catal. B: Environ.* 270 (2020), 118855, <https://doi.org/10.1016/j.apcatb.2020.118855>.
- [49] R. Zhu, Y. Zhu, H. Xian, L. Yan, H. Fu, G. Zhu, Y. Xi, J. Zhu, H. He, CNTs/ferrihydrite as a highly efficient heterogeneous Fenton catalyst for the degradation of bisphenol A: The important role of CNTs in accelerating Fe(III)/Fe(II) cycling, *Appl. Catal. B: Environ.* 270 (2020), 118891, <https://doi.org/10.1016/j.apcatb.2020.118891>.
- [50] R. Gao, L. Pan, H. Wang, X. Zhang, L. Wang, J. Zou, Ultradispersed nickel phosphide on phosphorus-doped carbon with tailored d-band center for efficient and chemoselective hydrogenation of nitroarenes, *ACS Catal.* 8 (2018) 8420–8429, <https://doi.org/10.1021/acscatal.8b02091>.
- [51] Z. Chen, Y. Song, J. Cai, X. Zheng, D. Han, Y. Wu, Y. Zang, S. Niu, Y. Liu, J. Zhu, X. Liu, G. Wang, Tailoring the d band centers enables Co₄N nanosheets to be highly active for hydrogen evolution catalysis, *Angew. Chem. Int. Ed.* 57 (2018) 5076–5080, <https://doi.org/10.1002/anie.201801834>.